universität
wien

MASTERARBEIT / MASTER'S THESIS

Titel der Masterarbeit / Title of the Master's Thesis

"Sensitivity of Dark Matter direct detection experiments to a cosmological relativistic background through electron recoils"

verfasst von / submitted by

Christina Xeni, BSc

angestrebter akademischer Grad / in partial fulfilment of the requirements for the degree of

Master of Science (MSc)

Wien, 2018 / Vienna, 2018

Studienkennzahl lt. Studienblatt / degree programme code as it appears on the student record sheet:	A 066 876
Studienrichtung lt. Studienblatt / degree programme as it appears on the student record sheet:	Master studies in Physics
Betreut von / Supervisor:	Dr. Josef Pradler
Mitbetreut von / Co-supervisor:	Univ.-Prof. Dr. André H. Hoang

Abstract

In this thesis we focus on the direct detection of dark particles coming from the decay of an unstable dark matter progenitor. Specifically we focus on the scattering of a dark particle χ, which could either be a Dirac fermion or a scalar, on bound atomic electrons of target atoms in dark matter direct detection experiments. This interaction is supposed to be mediated by a hidden sector U(1) vector boson, which mixes kinetically with the Standard Model photon. We compute contributions to the event rate coming from galactic and extragalactic particles sources that result from the decay of an unstable dark matter progenitor. Taking into account present constraints on the elastic χe cross-section we determine regions of parameter space, which yield visible event rates.

Zusammenfassung

In dieser Arbeit konzentrieren wir uns auf die direkte Detektion dunkler Teilchen, die aus dem Zerfall eines instabilen Vorläufers der Dunklen Materie stammen. Insbesondere konzentrieren wir uns auf die Streuung eines dunklen Teilchens χ, das entweder ein Dirac-Fermion oder ein Skalar sein kann, an gebundenen Atomelektronen von Zielatomen in direkten Detektionsexperimenten der Dunklen Materie. Diese Wechselwirkung soll durch einen Vektorboson eines verborgenen U(1) Sektors vermittelt werden, der sich kinetisch mit dem Standardmodell Photon mischt. Wir berechnen Beiträge zur Ereignisrate aus galaktischen und extragalaktischen Teilchenquellen, die aus dem Zerfall eines instabilen Vorläufers der Dunklen Materie resultieren. Unter Berücksichtigung der bestehenden Limiten des elastischen χe - Wirkungsquerschnitts bestimmen wir Bereiche des Parameterraums, die sichtbare Ereignisraten ergeben.

Contents

List of Figures

Chapter 1

Fundamentals

1.1 The Standard Cosmological Model

Our Universe appears to be described well by a Hot Big Bang model known as ΛCDM, where Λ stands for a Universe with a cosmological constant and CDM stands for a Universe with a Cold Dark Matter component. The former is associated with dark energy and is responsible for the observed late-time accelerated expansion of the Universe, while the latter suggests that the dark matter (DM) component is non-relativistic (i.e. cold). Mathematically, our Universe is described by Einstein's field equations of General Relativity, which is a set of 10 partial differential equations, summarised into one tensor equation

$$G_{\mu\nu} - g_{\mu\nu}\Lambda = 8\pi G T_{\mu\nu}, \tag{1.1}$$

where $G_{\mu\nu}$ is the Einstein tensor, describing the geometry of spacetime and $T_{\mu\nu}$ is the stress-energy tensor, describing the energy content of the Universe; G is Newton's gravitational constant and $g_{\mu\nu}$ is the metric tensor. If we solve Einstein's equations for a homogeneous and isotropic Universe, that is a Universe that has no preferred direction[1], one obtains Friedmann's first equation from the 00 component of (1.1)

$$\left(\frac{\dot{a}}{a}\right)^2 + \frac{K}{a^2} - \frac{\Lambda}{3} = \frac{8\pi G}{3}\rho(t), \tag{1.2}$$

where $a = a(t)$ is the only dynamical parameter, called the "scale factor", which describes the relative expansion of our Universe. By definition the scale factor for today is $a(t_0) \equiv a_0 = 1$, where $t_0 \approx 13.7$ Gyr [1] is today's cosmological time (the age of the Universe). The first term in (1.2), $\dot{a}/a \equiv H$, is called the Hubble rate and

---

[1] Our Universe on smaller scales is inhomogeneous, which has led to structure formation, however on larger scales a homogeneous and isotropic Universe is a valid approximation.

$$
\begin{aligned}
\Omega_\Lambda &= 0.685 \\
\Omega_{\rm cdm} &= 0.265 \\
\Omega_{\rm b} &= 0.0499 \\
\Omega_\nu &= 5.5 \times 10^{-3} \\
\Omega_\gamma &= 5.5 \times 10^{-5}
\end{aligned}
$$

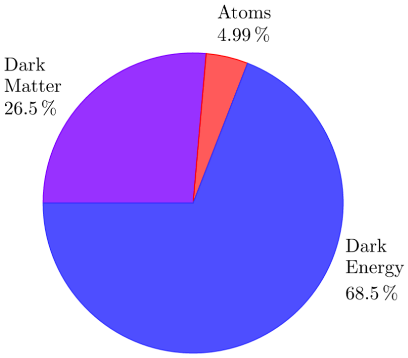

Figure 1.1: The current energy budget of the Universe. The values are inferred from CMB anisotropy measurements by COBE, WMAP and Planck experiments [1].

describes the expansion rate of the Universe. It has units of velocity per distance. The current value is called the Hubble constant,

$$H_0 = 100\, h\, \mathrm{km\, s^{-1}\, Mpc^{-1}}, \tag{1.3}$$

where $h = 0.676$ [1] is the so called scaled Hubble parameter. K describes the curvature of the Universe. Cosmic microwave background (CMB) anisotropies measurements reveal that the Universe is flat to high accuracy, so that this term in (1.2) can be ignored ($K = 0$). For a flat Universe, one defines a critical density $\rho_c(t)$, which describes the total energy density in the Universe at a cosmic time t. The total energy density includes a constant density ρ_Λ, associated with dark energy through the cosmological constant in (1.2) and a time-dependent density of matter and radiation $\rho(t) = \rho_m(t) + \rho_r(t)$. The matter density includes both an energy density for cold dark matter $\rho_{\rm cdm}$ and an energy density for regular matter, comprised mostly of baryons ρ_b.

The ratio of an energy density ρ_i to the critical density, is defined as the density parameter, which gives the percentage of each form of matter, energy, particle species etc. in the Universe

$$\Omega_i \equiv \frac{\rho_i}{\rho_c}, \quad \text{for } i = \mathrm{cdm},\, b,\, \gamma,\, \Lambda,\, \nu, \ldots \tag{1.4}$$

The current energy budget, obtained from measurements of the CMB anisotropies [1] can be seen in Fig. (1.1). Knowing how the various energy densities scale with time, and the fact that the sum of all energy density parameters for a flat Universe equals one, we can express the Hubble rate in terms of today's value as follows

$$H^2 = H_0^2 \left[\Omega_\Lambda + \Omega_m \left(\frac{a_0}{a} \right)^3 + \Omega_r \left(\frac{a_0}{a} \right)^4 \right]. \tag{1.5}$$

Instead of working with cosmic time, it is often more convenient to work in terms of redshift z, defined as follows

$$1 + z \equiv \frac{a_0}{a}. \tag{1.6}$$

Following this definition, we can exchange the time dependence of the Hubble parameter (1.5) with a redshift dependence,

$$H(z)^2 = H_0^2 \left[\Omega_\Lambda + \Omega_m (1+z)^3 + \Omega_r (1+z)^4\right]. \tag{1.7}$$

The redshift's value today is zero and becomes larger at earlier times. To express the cosmological time in terms of the redshift, one needs to differentiate (1.6) and divide by the scale factor, yielding the Hubble parameter

$$\frac{\dot{a}(z)}{a(z)} = H(z) = -\frac{\dot{z}}{1+z} \Rightarrow dt = -\frac{dz}{(1+z)H(z)}. \tag{1.8}$$

To find the cosmic time t at redshift z, we integrate both sides for a time interval t to today t_0, corresponding to redshift z and $z_0 = 0$

$$\int_t^{t_0} dt' = t_0 - t(z) = \frac{1}{H_0} \int_z^{z_0} \frac{dz'}{(1+z')\sqrt{\Omega_\Lambda + \Omega_m (1+z')^3}} \tag{1.9}$$

where the approximation $\Omega_r \approx 0$ has been used. The solution for the cosmic time at redshift z is then

$$t(z) = \frac{2}{3H_0\sqrt{\Omega_\Lambda}} \ln\left[\frac{\sqrt{\kappa + (1+z)^3} + \sqrt{\kappa}}{\sqrt{(1+z)^3}}\right], \tag{1.10}$$

where $\kappa = \Omega_\Lambda/\Omega_m \simeq 2.24$.

1.2 Evidence of Dark Matter

One of the strongest historical evidences for the existence of dark matter is given by galaxy rotation curves, where the orbital velocities of stars within the galaxy are plotted against their distance from the galactic center (GC). The underlying relation between orbital velocities and distance to the GC is given by Newtonian dynamics,

$$v(r) = \sqrt{\frac{GM(r)}{r}}, \tag{1.11}$$

where $M(r)$ is the total mass distribution within a radius r. There are two regions of interest: close to and outside the GC. In the former, stars have a constant mass

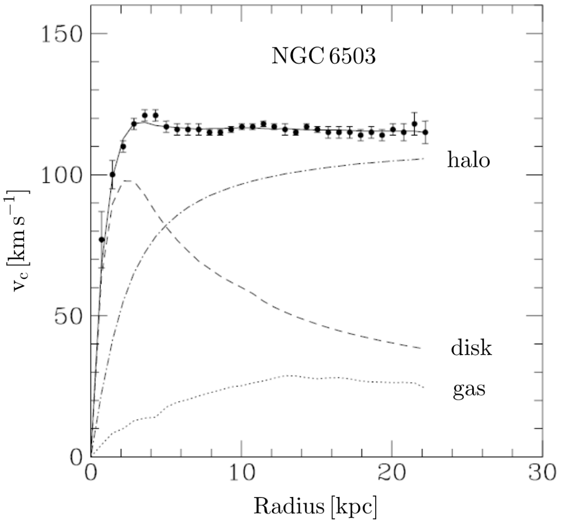

Figure 1.2: Rotation curve of the spiral galaxy NGC 6503 by [2]. The observed curve (solid line) shows a nearly constant velocity with increasing radius, contrary to what is expected (dashed line) for the visible components following Kepler's third law. The dash-dot and the dotted curves show the rotation curves of the individual components dark matter halo and gas respectively.

density ρ_0 and a mass distribution $M(r) = \rho_0 4\pi r^3/3$. One therefore expects that stars close to the GC have orbital velocities $v(r) \propto r$. In the latter, a star has a velocity $v(r) \propto 1/\sqrt{r}$. Therefore one would naturally expect the velocity curve to increase for stars close to the GC and fall for stars on the outskirts of the galaxy. However, observations showed that velocities for those stars that are on the outskirts are nearly constant, which indicates that there is additional "dark" matter that creates a greater gravitational potential to support a faster stellar movement. Such a curve is shown in Fig. (1.2), for the spiral galaxy NGC 6503 [2].

Gravitational lensing is a method used to determine the mass of an astronomical object, called "lens". Einstein's general relativity reveals that light bends in the presence of a massive object, yielding a corresponding relation between the deflection angle and mass of the lens. A prime example of this evidence is the observation of a system called the Bullet-Cluster, which is a result of two colliding galaxy clusters and has been observed in 2006 by the Hubble space telescope [3]. During their collision, the stellar components of both clusters passed by each other without interacting, contrary to the interacting fluid-like gas and dust. In the absence of a DM component, the mass distribution should then follow the main mass contributor as shown in the right image of Fig. (1.3). The interacting plasma emits X-rays, which are detected and reveal their position relative to the stellar components as shown in the left image. Weak gravitational lensing revealed the mass distribution within the

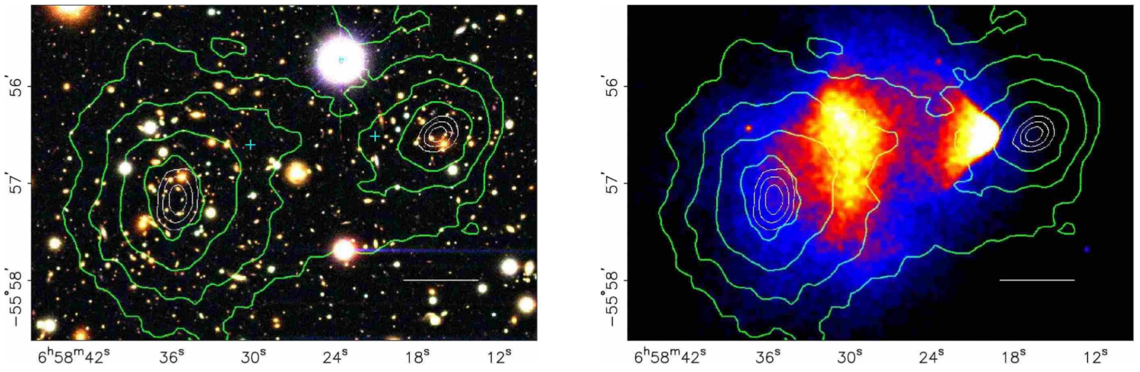

Figure 1.3: The stellar components of the Bullet-Cluster [3] is shown (left), being spatially separated to the colluded plasma, as X-ray emission reveals, in the blue, red and yellow regions (right). In both images the green contour lines show the mass distribution obtained by weak gravitational lensing. The inner contours have higher mass concentration than the outer.

cluster, depicted with the green contour lines. These lines show that the main mass contributor is not the hot plasma, but rather a collisionless non-luminous matter, shown to be present amidst the stellar components, with the highest concentration being towards the center of each cluster.

Finally, CMB anisotropy measurements not only laid further evidence for the existence of DM, it also provided precise information on its abundance in the Universe. Even though the CMB spectrum, as has been measured by COBE and later by WMAP and Planck satellites, shows a nearly perfect black body spectrum at a mean temperature of $T_0 = 2.725$ K [4], more precise measurements reveal small fluctuations at the level of $\sim$ μK. These temperature fluctuations originate from acoustic oscillations. The temperature map can be expanded in spherical harmonics, with multipoles l, forming a power spectrum of temperature anisotropies as shown in Fig. (1.4). The measured anisotropies (blue dots) are then fitted within a given cosmological model (red line). The position of the peaks, as well as their relative heights, can reveal information about the curvature of the Universe, the total matter density Ω_m and the baryon density Ω_b. The difference between Ω_m and Ω_b yields the corresponding density for CDM, which today is [1]

$$\Omega_\mathrm{cdm} = 0.265(11). \tag{1.12}$$

Altogether, the evidence of the existence of DM in the Universe is well established. The exact particle nature of DM is still an open question.

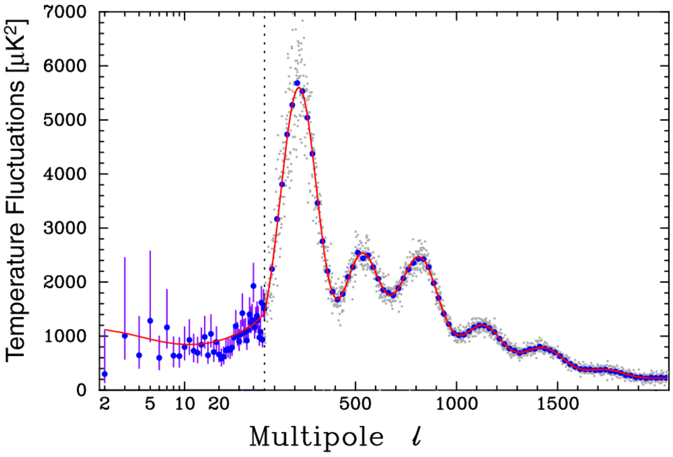

Figure 1.4: Power spectrum of the CMB as measured by the Planck satellite [5].

1.3 Dark Matter candidates

A viable DM candidate must fulfill certain requirements according to the cosmological observations made thus far. To summarize them, these are some important requirements for such a candidate:

1. According to the CMB anisotropy measurements, the matter density of the Universe is dominated by a **non-baryonic** DM component. A successful candidate must therefore yield a density in agreement with the measured relic abundance Ω_{cdm} as in Eq. (1.12).

2. It should be **dark**, since it hasn't been ever physically observed, other as through gravitation. For a particle to be non-luminous it must therefore be (largely) electrically neutral.

3. Because of the long-lived large-scale structures observed in the Universe, at least on cosmological time scales, DM must be **stable**.

4. Structure formation as observed in galaxies and galaxy clusters suggest that dark matter is **cold**. Cold means that the DM particle has been non-relativistic by the time of structure formation. N-body simulations show that hot DM can not form galaxies as we observe them and would thus lead to a different Universe with a different primordial fluctuation spectrum.

From these requirements, one may start excluding some of the known particles or objects that could make a DM candidate. Baryonic candidates, which have been previously considered as an explanation to the missing mass problem, such as massive compact halo objects (MACHOS) [6]-[7] must also hereafter be excluded. Under this category fall, for example, black-hole remnants, white dwarfs, brown dwarfs, neutron stars or in short stellar remnants that no longer radiate light as they go through the process of stellar death. By this paradigm, all baryons should be excluded. Because of the second requirement, charged leptons are excluded, since they couple through their charge to the electromagnetic force. The third requirement excludes furthermore the SM neutral gauge bosons as well as the Higgs boson from the possible candidates, since they have a very short lifetime.

The only remaining DM particle candidate in the SM are the neutrinos. However, neutrinos do no make a good DM candidate because of their small mass. Cosmological measurements, including BOSS Lyα and Planck CMB, constraint the total sum of the neutrino masses to $\Sigma_i \nu_i < 0.12$ eV (95% C.L.) [8]. This therefore yields a cosmological abundance for the neutrino species, which is significantly less than the relic abundance of DM.

In conclusion, none of the SM particles can make a good DM candidate. Such a particle with the requirements mentioned in this section has to be sought in new models of physics beyond the SM. Extensions of the SM of particle physics exist, including one of the largest class of DM candidates, such as the Weakly Interacting Massive Particles (WIMPs). A huge success of WIMPs as a viable candidate of DM, comes from the fact that it obtains the correct relic abundance, if we assume that they are mostly (or exclusively) produced through thermal production in the early Universe.

1.4 WIMP Dark Matter

The process of thermal production in the early Universe causes a “freeze out” of the particle number density of a certain species. Because particles have limited interaction range, a relic abundance can be formed when the annihilation rate Γ of the species becomes smaller than the expansion rate H of the Universe. In this case, because of the expansion, particles and antiparticles are “too far” from each other to interact, which causes the annihilation process to stop. As can be seen in Fig. (1.5) the particle density departures from its thermal equilibrium value and freezes-out at the point when $\Gamma \sim H$ with the release of a relic abundance.

Assuming only thermal production, one can estimate the DM relic abundance by solving the Boltzmann equation that describes the evolution of the particle number density of the DM particle species, ψ, as follow

$$\dot{n}_\psi + 3Hn_\psi = -\langle \sigma_{\rm ann} v \rangle \left[(n_\psi)^2 - (n_\psi^{\rm eq})^2 \right] , \tag{1.13}$$

where $\langle \sigma_{\rm ann} v \rangle$ is the thermally averaged annihilation cross-section for the process

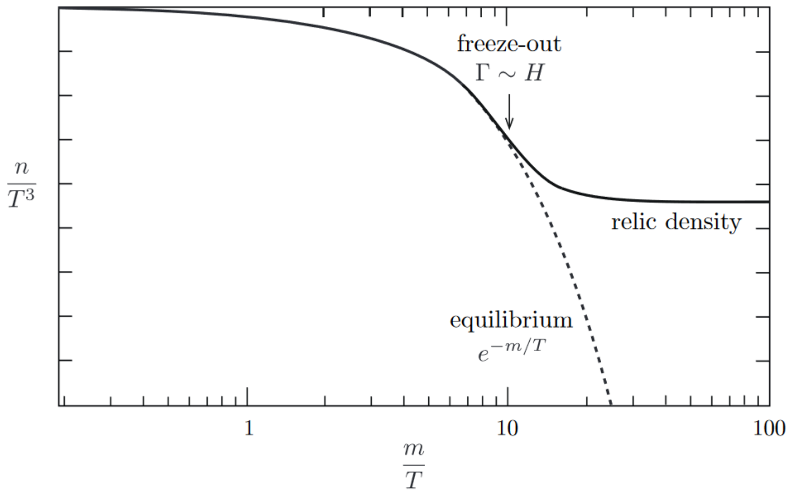

Figure 1.5: Behaviour of particle number density versus inverse temperature in an expanding Universe (solid line) with a freeze out starting when $\Gamma \sim H$. In a hypothetical static Universe (that still cools) the number density would keep decreasing exponentially (dashed line). Figure taken from [9].

$\psi\bar{\psi} \rightarrow \chi\bar{\chi}$ and n_{ψ}^{eq} is the particle's density at thermal equilibrium. χ is a lighter particle, that can either be a SM particle, or another particle in the dark sector. The second term in the left-hand side of (1.13) is a dilution term caused by the expansion of the Universe.

To estimate the relic abundance, the Boltzmann equation needs to be solved, while $\langle\sigma_{\text{ann}} v\rangle$ needs to be evaluated as a function of temperature. Various numerical recipes exist to estimate the relic abundance. In the simplest cases, the dependence on the mass of the DM particle drops from the estimation of the relic abundance, [10]

$$\Omega_{\text{cdm}} \simeq \frac{0.217 \times 10^{-36}\,\text{cm}^2}{\langle\sigma_{\text{ann}} v\rangle}. \tag{1.14}$$

The relic density is thus inversely proportional to the annihilation cross-section. The latter points to be of the order of a typical weak scale interaction ($\simeq 10^{-36}\,\text{cm}^2$) to achieve a relic density with the observationally inferred value (1.12). This is often called the “WIMP miracle”.

1.5 Dark Matter distribution

According to the observations laid out in the previous section, non-baryonic, collisionless DM dominates the mass budget of galaxies and other bigger structures, like galaxy clusters. DM resides in halos and their formation can be understood in the context of cosmological perturbations in the early Universe. Those inhomogeneities led to structure formation, which led them to grow with time, since over-dense regions pulled matter towards them, a process referred to as gravitational instability. In early times density perturbations grow linearly until they reach a critical density, after which they collapse to form DM halos [11].

The structure of a DM halo has been explored using numerical simulations. As a first approximation it is taken to be a spherical object with mass distribution described by a density profile, $\rho(r)$. One such model uses a double power-law density distribution profile, which is parametrized as follows [12]

$$\rho(r) = \rho_0 \left(\frac{r}{r_0}\right)^{-\gamma} \left[1 + \left(\frac{r}{r_0}\right)^{\alpha}\right]^{(\gamma-\beta)/\alpha}, \tag{1.15}$$

with a certain set of parameters (α, β, γ). This double power-law spectrum yields $\rho(r) \propto r^{-\gamma}$ for small radii (close to the GC) and $\rho(r) \propto r^{-\beta}$ for larger radii. One such density profile is given by the parameter set $(\alpha, \beta, \gamma) = (1, 3, 1)$, which is called NFW [13]-[14] obtained from high resolution N-body simulations. Other groups with different set of parameters have also been proposed, like the Moore profile [15] with $(\alpha, \beta, \gamma) = (1.5, 3, 1.5)$, which comes in agreement with the proposed NFW profile for large radii with $\rho(r) \propto r^{-3}$, but for smaller radii it predicts a steeper asymptotic slope than the NFW profile with $\rho(r) \propto r^{-1.5}$. For the rest of this work I adopt the NFW density profile, given by the power law

$$\rho_{\mathrm{NFW}}(r) = \frac{\rho_s}{(r/r_s)(1 + r/r_s)^2}, \tag{1.16}$$

where ρ_s is the so-called scale radius and r_s is a parameter that depends from halo to halo. Later, when we specialize to the Milky Way, we use the values $r_s = 20$ kpc and $\rho_s = 0.35\,\mathrm{GeV/cm^3}$ for a DM density in the solar neighborhoud of $\rho_\odot \approx 0.4\,\mathrm{GeV/cm^3}$ [16]-[17].

1.5.1 Local density and velocity distribution

Two important quantities determine the outcome of particle rates in direct detection experiments, the local DM density $\rho_\odot$ at the position of the solar system, $R_\odot = 8.5\,\mathrm{kpc}$ [18] away from the GC and the DM velocity distribution $f(\vec{v})$. Observing the rotational curves of the Milky way can give an estimate on both of these quantities. For simplicity, a model called the Standard Halo Model (SHM) is used for the determination of these quantities, where the local DM distribution is taken to be smooth and virialized, with an average density of $\rho_\odot \approx 0.4\,\mathrm{GeV/cm^3}$ as discussed previously. This estimate can vary depending on the density profile and initial conditions used to estimate it, but this average value is going to be used in this work. The

SHM also assumes a spherically symmetric and isothermal dark matter distribution [19] around the galactic centre with a Maxwellian velocity distribution given by

$$f(\vec{v}) = \frac{1}{N_{\mathrm{esc}}}\, e^{-\vec{v}^{\,2}/v_0^2}, \tag{1.17}$$

where $v_0 = 220\,\mathrm{km/s}$ [18] is the mean DM velocity. The factor N_{esc} is a normalization constant, which can be calculated by taking into account the galactic escape velocity v_{esc} in the rest frame of the DM halo,

$$\begin{aligned} N_{\mathrm{esc}} &= \int_0^{2\pi} d\phi \int_{-1}^{1} d\cos\theta \int_0^{v_{\mathrm{esc}}} e^{-\vec{v}^{\,2}/v_0^2}\, d^3v \\ &= (\pi v_0^2)^{3/2}\left[\mathrm{erf}\left(\frac{v_{\mathrm{esc}}}{v_0}\right) - \frac{2}{\sqrt{\pi}}\frac{v_{\mathrm{esc}}}{v_0} e^{-v_{\mathrm{esc}}^2/v_0^2}\right], \end{aligned} \tag{1.18}$$

where erf denotes the error function. The escape velocity yields a maximum velocity, above which WIMPs are no longer gravitationally bound to the galactic potential. It is estimated using high velocity stars and yields a mean value of $v_{\mathrm{esc}} = 544\,\mathrm{km/s}$ [20].

1.5.2 Annual modulation

The Maxwellian distribution function in (1.17) is defined in the rest frame of the DM halo. The distribution as is measured from Earth, should be taken in the rest frame of the laboratory and in fact varies throughout the year due to Earth's motion around the Sun. Therefore, the distribution in the rest frame of the detector is related to (1.17) through a Galilean boost

$$f(\vec{v}, t) = f(\vec{v} + \vec{v}_{\mathrm{E}}(t)), \tag{1.19}$$

where $\vec{v}_{\mathrm{E}}(t)$ is the Earth's velocity in the galactic rest frame and is parametrized as follows

$$\vec{v}_{\mathrm{E}}(t) = \vec{v}_{\mathrm{LSR}} + \vec{v}_{\mathrm{pec}} + \vec{v}_{\oplus}(t), \tag{1.20}$$

where $\vec{v}_{\mathrm{LSR}}$ is the velocity of the Local Standard of Rest, meaning the velocity at which the material in the neighbourhood of the Sun moves around the GC and is parametrize as $\vec{v}_{\mathrm{LSR}} = (0, v_0, 0)$ in galactic coordinates. All the velocities are given in galactic coordinates $(\hat{x}, \hat{y}, \hat{z})$, where $\hat{x}$ points towards the GC, $\hat{y}$ towards the direction of the local disk rotation and $\hat{z}$ is perpendicular to the galactic plane disk (i.e. the direction of the galactic North pole). Further $\vec{v}_{\mathrm{pec}}$ is the Sun's peculiar velocity with respect to the LSR, with an estimate $\vec{v}_{\mathrm{pec}} \approx (11, 12, 7)\,\mathrm{km/s}$ [21]. Finally the Earth's velocity, neglecting the ellipticity of the orbit, can be parametrized as follows [22]

$$\vec{v}_\oplus(t) \approx v_\oplus[\hat{\epsilon}_1 \cos\omega(t-t_1) + \hat{\epsilon}_2 \sin\omega(t-t_1)], \tag{1.21}$$

where $v_\oplus = 29.8\,\text{km/s}$ is the Earth's velocity around the Sun, $\omega = 2\pi/\text{year}$ is the angular velocity and the vectors $\hat{\epsilon}_1$ and $\hat{\epsilon}_2$ give the directions of the Earth's motion at the Spring equinox (20 March or $t_1 = 79\,\text{days}$) and Summer solstice (21 June or $t_1\,\text{year} = 172\,\text{days}$) respectively with

$$\begin{aligned}\hat{\epsilon}_1 &= (0.9931, 0.1170, -0.01032),\\ \hat{\epsilon}_2 &= (-0.0670, 0.4927, -0.8676).\end{aligned} \tag{1.22}$$

The galactic velocity of Earth varies throughout the year because of Earth's yearly orbit around the Sun. There is a maximum velocity that is achieved at the time of the year, at which the orbital velocity is maximum, and this is on June 2 or $t = 153\,\text{days}$. Therefore the magnitude of $v_\text{E}(t)$ can be approximately written as [22]

$$\begin{aligned}v_\text{E}(t) &\approx v_\odot + v_\oplus b\cos\omega(t-153),\\ &\approx 232 + 15\cos\left(2\pi\frac{t-153}{365}\right)\,\text{km/s},\end{aligned} \tag{1.23}$$

where $b = \sqrt{(\hat{\epsilon}_1\cdot\hat{v}_\odot)^2 + (\hat{\epsilon}_2\cdot\hat{v}_\odot)^2}$ and $v_\odot = |\vec{v}_\text{LSR} + \vec{v}_\text{pec}|$.

1.6 Dark matter searches

In order to draw definite conclusions about the properties of dark matter, like its mass or couplings, one has to first detect it. There are three methods of experimental searches: direct detection, indirect detection and searches at colliders. The process that each detection method undergoes is outlined in Fig. (1.6), where the arrow denotes the flow of time for an unknown interaction between two DM and two SM particles.

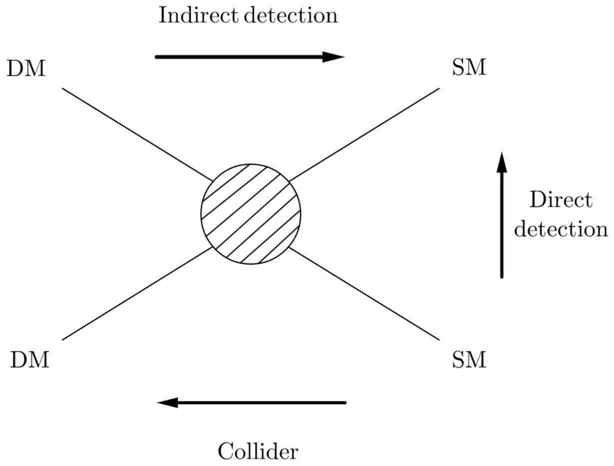

Figure 1.6: Diagrammatic illustration of an unknown interaction (lined blob) between two DM and two SM particles. The arrows point in the direction of time for each detection method.

1.6.1 Direct detection

A direct detection of DM is, as the name suggests, a detection of a scattering event of a DM particle through its direct impact with a terrestrial DM detector. DM particles originating from the DM halo of our galaxy pass through Earth continually. The goal of direct detection experiments is thus to build large enough or sensitive enough detectors, placed underground to avoid the inevitable cosmic radiation, to enable such a weak interaction to be observable. This is a similar framework to that of neutrino detection experiments. In contrast to neutrino experiments however, that primarily detect MeV and above energy deposits, DM experiments search for keV energy deposits.

The energy transfer due to the interaction between the DM particle with the detector material is mediated through three different signals, based on the detector technology used. Cryogenic detectors operating at ultra-low temperatures are able to detect signals in form of heat (phonons). Noble liquid gas detectors, specifically if made with a dual phase technology, allow the detection of low energetic nuclear recoils, via simultaneous detection of the ionization through the release of electrons and scintillation photons through relaxation of excited states. This offers the unique advantage of background discrimination, since the signal characteristics vary from particle to particle as depicted in Fig. (1.7).

In most direct detection experiments, that focus on WIMP DM models, only signals that cause nuclear recoils are being registered and are expected to be in the energy range of 1–100 keV for DM masses of a few hundred GeV to TeV [23]. Electronic recoils are generally being rejected as a background signal, caused primarily

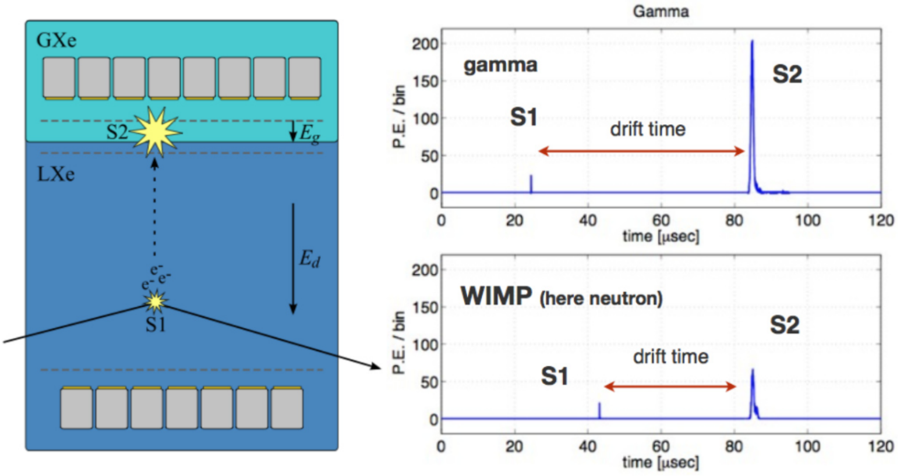

Figure 1.7: (Left) The schematic working mechanism of the dual phase TPC, where an interaction takes place in the LXe, that releases both ionized electrons that drift towards the GXe through an applied electric field (which prompts a delayed S2) and scintillation photons through relaxation of excited states that drift towards the cathode prompting S2. (Right) Scheme of the signal intensities for nuclear (up) and electronic recoil (down). Picture taken from [27].

by natural radioactivity of detector components.

Redundant background rejection schemes are a key prerequisite of all the recent direct detection experiments, along with a detector threshold of nuclear recoils of a few keV. The choice of liquid Xenon (LXe) has proven to be a suitable target. Experiments using this material include the XENON Dark Matter Project in Gran Sasso National Laboratory (GSNL) in Italy [24], the Large Underground Xenon (LUX) Experiment at the Sanford Underground Research Facility in the USA [25], the ZEPLIN-III dark matter experiment at the Boulby Underground Laboratory in the UK [26], to name a few. All of these experiments have run through multiple stages with increasing detector target mass and improved detector sensitivity. They have established strong constraints on WIMP DM-nucleon interactions in the DM mass ranges of $\mathcal{O}$(1–100 GeV).

Dark matter experiments using LXe

A feature that most of the direct detection experiments with LXe share is the use of a dual-phase, meaning both LXe and gas xenon (GXe), time projection chamber (TCP). The dual phase technology allows the detection of low energetic nuclear recoils, via simultaneous detection of the ionization, through primary scintillation in LXe (S1) and secondary scintillation in GXe (S2). The ratio $S2/S1$ provides an event-by-event discrimination between nuclear and electron recoils, since these two

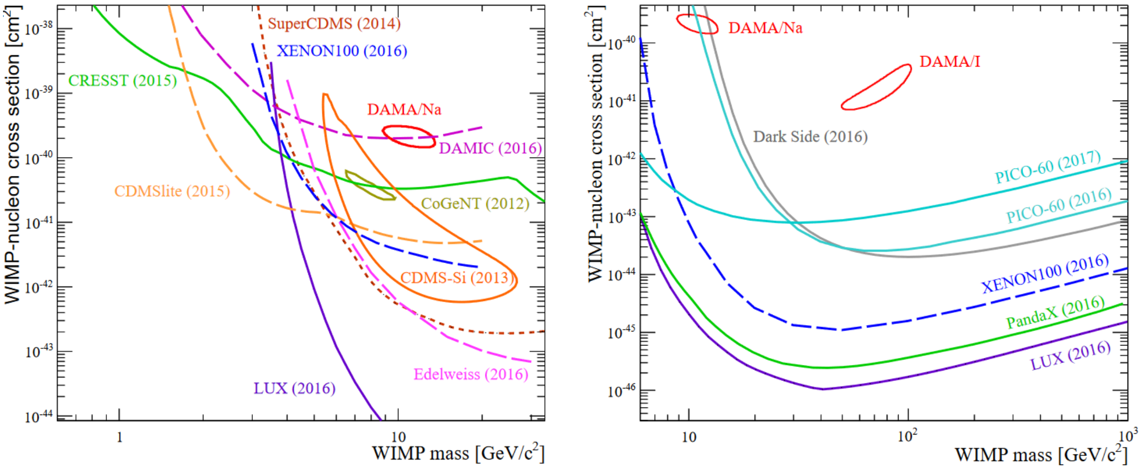

Figure 1.8: Signal indications (closed contours) and exclusion limits (curves) for low WIMP masses (left) and high WIMP masses (right). Plots are from [33].

are different. This principle is illustrated in Fig. (1.7) taken from [27].

The first TPC prototype of the XENON project labeled XENON10 had used 15 kg of LXe and analysed a data obtained in 58.6 live days. The first results [28] set a new upper limit for the WIMP-nucleon spin-independent cross-section. Based on their success, an upgraded version of the project has been designed to uphold 10 times more mass than XENON10 and thus is labeled as the XENON100 project. XENON100 had 3 runs that summed up to 477 live days between 2010 and 2014 [29–31]. As of 2016, by the end of the second run, according to their report [32] they had established the world's best upper limits on the spin-independent (SI) and spin-dependent (SD) coupling of WIMPs to nucleons and neutrons, respectively. These limits, as can be seen in Fig. (1.8), have excluded regions of parameter space that have been previously unexplored, including some preferred by SUSY models.

1.6.2 Indirect detection

Searching DM indirectly means detecting products of its annihilations or its decay. Among the products that are typically being looked for are cosmic neutrinos, γ-rays, positrons, antiprotons and antideuterons, which arise as primary or secondary products in DM annihilations or decays. Looking at those fluxes, one can distinguish between products coming from annihilations against those that come from decays. The incoming flux of a DM annihilation will be proportional to the square of the DM distribution $\rho_{\rm DM}$ times a thermally averaged annihilation cross-section,

$$\phi_{\rm ann} \sim \rho^2_{\rm DM} \langle \sigma_{\rm ann} v \rangle, \tag{1.24}$$

while for a decaying DM product, the flux is proportional to its matter distribution and inversely proportional to its decay time,

$$\phi_{\text{decay}} \sim \frac{\rho_{\text{DM}}}{\tau_{\text{DM}}}. \tag{1.25}$$

Therefore good places to look for are dense DM regions like the GC or dwarf spheroid galaxies.

There are several experiments dedicated to indirect DM searches that have specialised on detecting specific annihilation products and have thus put limits on certain DM properties. The neutrino detector IceCube searches for muon neutrino signatures from certain models of DM and has obtained upper limits on the annihilation rate [34]. For DM induced γ-rays, Fermi-LAT has produced cross-section limits for generic DM candidates, from both extragalactic and galactic sources [35]. The satellite-borne experiment PAMELA measures ratios of matter to antimatter fluxes and compares them with theoretical predictions [36].

1.6.3 Collider searches

Finally, a third method of DM detection is its production at colliders. Collider searches may include scenarios where DM is produced directly from standard model particle interactions, or indirectly through the decay of intermediary particle states. DM will likely transverse the detector undetected and will thus be registered as missing energy and momentum. A possible signal would be the production of DM pair $\chi\bar{\chi}$ with an associated production of jets, as in the following process

$$pp\,(p\bar{p}) \;\rightarrow\; \chi\bar{\chi} + \text{jets}. \tag{1.26}$$

Because of the weekly interacting nature of neutrinos, similar processes, through the production of Z^0 and $W^{\pm}$ gauge bosons, can be considered background processes such as the following

$$\begin{aligned} pp\,(p\bar{p}) \;&\rightarrow\; \nu\bar{\nu} + \text{jets}, \\ pp\,(p\bar{p}) \;&\rightarrow\; l^{-}\bar{\nu} + \text{jets, etc.} \end{aligned} \tag{1.27}$$

QCD backgrounds, such as the production of $t\bar{t}$ that decay into $W^{\pm}$ bosons, can also be considered a background process in colliders such as the LHC. Inclusive cross-sections for a given center of mass energy can then be calculated for signal and background processes within the framework of an effective field theory, such as described in [37].

Chapter 2

Dark matter and light mediators

2.1 Motivation

DM in conjunction with light, sub-GeV particles mediating the interaction between DM and SM is an often encountered scenario in the literature. A common assumption is that the mediator interacts with the SM through a kinetic mixing with the hypercharge $U(1)_Y$ gauge group. For example, as discussed in [38] and [39], a light force carrier can boost the annihilation cross-section of DM at low velocities. This so-called Sommerfeld enhancement [40] has been used to interpret the results in the positron fraction observed by PAMELA [41] and later by FERMI [42], [43] and AMS [44]. The Sommerfeld enhancement occurs if the force carrier distorts the wave function of the incoming DM particles due to the long range nature of the interaction. A schematic representation of this effect is shown in Fig. (2.1).

In the following we focus on a specific class of DM models characterised by a light mediator that kinematically mixes with the photon.

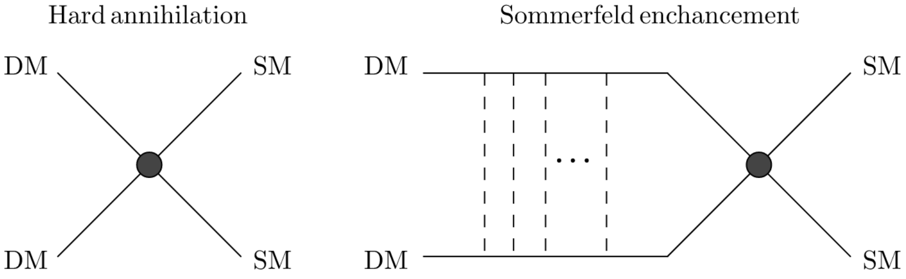

Figure 2.1: Annihilation of two DM particles into SM final states without (left) and with (right) Sommerfeld enhancement [45]. The dashed lines show the exchange of light mediators that occurs before the hard annihilation.

2.2 Toy model and Feynman rules

In order for DM to interact with SM particles, a vector particle, usually referred to in the literature as the “dark photon”, is introduced [46]. This model extends the SM gauge group by an Abelian group $U(1)_V$ with field strength tensor $V_{\mu\nu} = \partial_\mu V_\nu - \partial_\nu V_\mu$; $V_\mu(x)$ represents the dark photon field, which is allowed to kinetically mix with the photon [47]-[48]. The dark photon is further assumed to be massive. The origin of its mass can be due to a spontaneously broken symmetry by a dark higgs-like field or it can have other origins, as discussed in [49]. Since a UV completion of this model goes beyond the scope of this work, we argue in terms of a low energy effective theory, whose Lagrangian has the following form

$$\mathcal{L} = -\frac{1}{4}F_{\mu\nu}^2 - \frac{1}{4}V_{\mu\nu}^2 + \frac{\epsilon}{2}F_{\mu\nu}V^{\mu\nu} + \frac{1}{2}m_V^2 V_\mu V^\mu, \tag{2.1}$$

where m_V denotes the dark photon’s mass and ϵ is the kinetic mixing between the photon and the dark photon. If we assume a fermionic DM particle χ, then we add the following Lagrangian term

$$\mathcal{L}_\chi = \bar{\chi}(i\not{D} - m_\chi)\chi, \tag{2.2}$$

where $\not{D}$ is the covariant derivative $D_\mu(x) = \partial_\mu - ig_D V_\mu(x)$ and g_D the coupling of the DM particle to the dark photon field. In case of a scalar DM particle ϕ, we add a scalar Lagrangian term

$$\mathcal{L}_\phi = |D_\mu\phi|^2 - m_\phi^2|\phi|^2, \tag{2.3}$$

with a covariant derivative $D_\mu(x) = \partial_\mu - ig_S V_\mu(x)$, where g_S is the corresponding coupling of V_μ to the scalar field.

To begin calculating the cross section of an interaction such as in Fig. (2.2), we have to write down the Feynman rules for the interactions between the incoming DM particle and the dark photon, as well as the propagators of these fields. To extract the Feynman rules, we will decompose the Lagrangians (2.1)-(2.3) into free and interacting parts:

$$\begin{aligned}
\mathcal{L}_0 &= \frac{1}{2}A_\nu(g^{\mu\nu}\partial^2 - \partial^\mu\partial^\nu)A_\mu + \frac{1}{2}V_\nu(g^{\mu\nu}\partial^2 - \partial^\mu\partial^\nu)V_\mu + \frac{1}{2}m_V^2 V_\mu V^\mu \\
\mathcal{L}_I &= -\epsilon A_\nu(g^{\mu\nu}\partial^2 - \partial^\mu\partial^\nu)V_\mu \\
\mathcal{L}_0^\chi &= \bar{\chi}(i\not{\partial} - m_\chi)\chi \\
\mathcal{L}_I^\chi &= g_D\bar{\chi}\not{V}\chi \\
\mathcal{L}_0^\phi &= |\partial_\mu\phi|^2 - m_\phi^2|\phi|^2 \\
\mathcal{L}_I^\phi &= ig_S V^\mu(\phi^\dagger(\partial_\mu\phi) - (\partial_\mu\phi^\dagger)\phi) + g_S^2 V^\mu\phi^\dagger V_\mu\phi
\end{aligned} \tag{2.4}$$

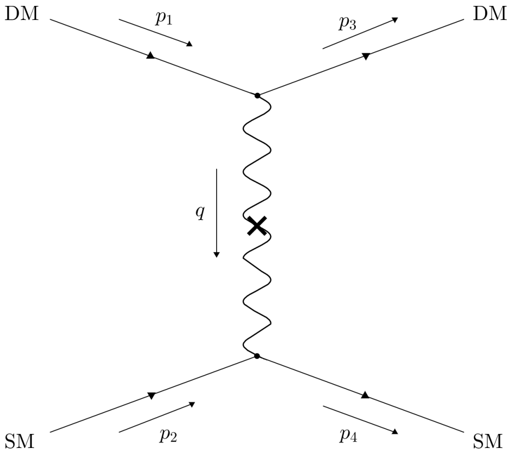

Figure 2.2: Tree level diagram for the scattering of a DM particle with an elementary SM particle. The interaction is mediated by a photon-dark photon interaction. The symbol × denotes the kinetic mixing between the photon and dark photon.

In the following, we denote with $i\tilde{\Delta}_{\mu\nu}(q)$ the propagators and with $i\tilde{\Gamma}_\mu$ the vertices in momentum space. The photon propagator in arbitrary gauge is for example given by

$$i\tilde{\Delta}_{\mu\nu}(q) = \frac{-i}{q^2 + i\epsilon}\left[g_{\mu\nu} - (1-\xi)\frac{q_\mu q_\nu}{q^2 + i\epsilon}\right]. \tag{2.5}$$

where $+i\epsilon$ is added to the denominator to fulfill the causality requirement for $q^2 \to 0$. The $q_\mu q_\nu$ piece does not contribute to a gauge invariant observable (like the one we are calculating), so that we can choose Feynman gauge with $\xi = 1$. The relevant propagators and vertices derived from the previous Lagrangians are summarized as follows:

1. Dark photon propagator

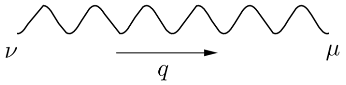

$$i\tilde{\Delta}^{V}_{\mu\nu}(q) = \frac{-i}{q^2 - m_V^2 + i\epsilon}\left(g_{\mu\nu} - \frac{q_\mu q_\nu}{m_V^2}\right)$$

2. Photon propagator

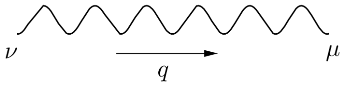

$$i\tilde{\Delta}^{A}_{\mu\nu}(q) = \frac{-ig_{\mu\nu}}{q^2 + i\epsilon}$$

3. Dark photon-photon kinetic mixing vertex

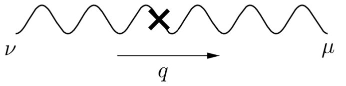

$$i\tilde{\Gamma}_{\mu\nu}(q) = i\epsilon(g_{\mu\nu}q^2 - q_\mu q_\nu)$$

4. Fermionic dark matter-dark photon vertex

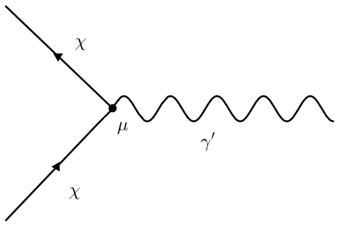

$$i\tilde{\Gamma}^{\chi}_{\mu} = ig_D\gamma_\mu$$

5. Scalar dark matter-dark photon vertex

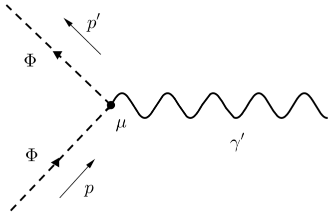

$$i\tilde{\Gamma}^{\Phi}_{\mu} = -ig_S(p + p')_\mu$$

In the following, two cases of 2-by-2 scattering is considered: fermionic DM scattering on a free electron and a scalar DM scattering on a free electron.

2.3 Elastic differential cross sections

The scattering amplitude corresponding to Fig. (2.2) can now be written with the help of the Feynman rules laid out in the previous section. The propagator between the interaction of DM and the interaction of electrons can be interpreted as the manifestation of 2 propagators (1)-(2) separated by a vertex due to the kinetic mixing (3). The scattering amplitude is then written as

$$i\mathcal{M} = [\bar{u}_{\sigma_4}(p_4) ie\gamma_\mu u_{\sigma_2}(p_2)]\frac{-i(g^{\mu\rho} - \frac{q^\mu q^\rho}{m_V})}{q^2 - m_V^2 + i\epsilon} i\epsilon(g_{\rho\sigma}q^2 - q_\rho q_\sigma)\frac{-ig^{\sigma\nu}}{q^2 + i\epsilon}[\bar{u}_{\sigma_3}(p_3) i g_D \gamma_\nu u_{\sigma_1}(p_1)]. \tag{2.6}$$

The calculation of the numerator in (2.6) has a simplification in that the only surviving element contracted with the right side of the equation is $\gamma^\mu q^2$. For an unpolarised cross section we need to average over initial spins, sum over final spins and then square the amplitude. The squared matrix element can be summarized as a product of two tensors, $\tilde{V}^{\mu\nu}$ the DM tensor and $L_{\mu\nu}$, the lepton tensor, as follows

$$\overline{|\mathcal{M}|^2} \equiv \sum_{\sigma_1,\sigma_2,\sigma_3,\sigma_4} \frac{1}{4}|\mathcal{M}|^2 = \frac{g_D^2 \epsilon^2 e^2}{4(q^2 - m_V^2)^2} L^{\mu\nu}\tilde{V}_{\mu\nu} \tag{2.7}$$

where the tensors can be calculated as follows

$$\begin{aligned} L^{\mu\nu} &= \sum_{\sigma_2,\sigma_4} \bar{u}_{\sigma_4}(p_4)\gamma^\mu u_{\sigma_2}(p_2)\bar{u}_{\sigma_2}(p_2)\gamma^\nu u_{\sigma_4}(p_4) \\ &= \mathrm{Tr}[\gamma^\mu(\not{p}_2 + m_e)\gamma^\nu(\not{p}_4 + m_e)] \\ &= 4(p_2^\mu p_4^\nu + p_2^\nu p_4^\mu + \frac{1}{2}q^2 g^{\mu\nu}) \\ \tilde{V}_{\mu\nu} &= \sum_{\sigma_1,\sigma_3} \bar{u}_{\sigma_3}(p_3)\gamma_\mu u_{\sigma_1}(p_1)\bar{u}_{\sigma_1}(p_1)\gamma_\nu u_{\sigma_3}(p_3) \\ &= 4(p_{1\mu}p_{3\nu} + p_{1\nu}p_{3\mu} + \frac{1}{2}q^2 g_{\mu\nu})\,. \end{aligned} \tag{2.8}$$

To shorten the notation of the averaged squared matrix element, we denote it with a horizontal bar. Combining both tensors, we finally obtain

$$\overline{|\mathcal{M}|^2} = \frac{4g_D^2\epsilon^2 e^2}{(q^2 - m_V^2)^2}[2(p_1 \cdot p_2)(p_3 \cdot p_4) + 2(p_1 \cdot p_4)(p_2 \cdot p_3) + q^2(m_\chi^2 + m_e^2)]. \tag{2.9}$$

We can further express this in terms of the standard Mandelstam variables s and t (see Appendices A),

$$\begin{aligned}\overline{|\mathcal{M}|^2} &= \frac{2g_D^2\epsilon^2e^2}{(t-m_V^2)^2}[(s-m_\chi^2-m_e^2)^2+(m_\chi^2+m_e^2-u)^2+2t(m_\chi^2+m_e^2)] \\ &= \frac{32\pi^2\epsilon^2\alpha\alpha_D}{(t-m_V^2)^2}[2(s-m_\chi^2-m_e^2)^2+2st+t^2], \end{aligned} \tag{2.10}$$

where α is the fine structure constant and α_D is a fine structure constant in the dark sector defined as $\alpha_D = g_D^2/4\pi$. We are interested in the differential cross section with respect to the CMS solid angle between the incoming and outgoing DM momenta, $d\Omega^*$, as defined in (A.19)

$$\frac{d\sigma}{d\Omega^*} = \frac{\overline{|\mathcal{M}|^2}}{64\pi^2 s} = \epsilon^2\alpha\alpha_D\frac{2(s-m_\chi^2-m_e^2)^2+2st+t^2}{2s(t-m_V^2)^2}, \tag{2.11}$$

where t is related to the CMS scattering angle θ^* as

$$t = 2m_\chi^2 - 2E_1^*E_3^* + 2p_1^*p_3^*\cos\theta^* = -2{p_1^*}^2(1-\cos\theta^*), \tag{2.12}$$

The boundary of the physical region for t for a fixed value of s is obtained through the requirement $-1 \leq \cos\theta^* \leq 1$, yielding

$$\begin{aligned} t &= 0 & &(\cos\theta^* = 1) \\ t &= -\frac{\lambda(s,m_\chi^2,m_e^2)}{s} & &(\cos\theta^* = -1) \end{aligned} \tag{2.13}$$

Finally for a scalar DM particle ϕ, the fermionic DM spinors $u_\sigma(p)$ in (2.6) are replaced with unity and our scattering amplitude contracted with the right side of the equation will yield

$$i\mathcal{M} = ig_S(p_1+p_3)_\mu\frac{\epsilon}{q^2-m_V^2+i\epsilon}[\bar{u}_{\sigma_2}(p_2)e\gamma^\mu u_{\sigma_4}(p_4)]. \tag{2.14}$$

Summing over spins σ_2 and σ_4, averaging over initial states and squaring the amplitude we obtain

$$\begin{aligned}\sum_{\sigma_2,\sigma_4}\frac{1}{2}\,|\mathcal{M}|^2 &= \frac{2\,\epsilon^2 e^2 g_S^2}{(q^2-m_V^2)^2}(p_1+p_3)^\mu(p_1+p_3)^\nu(p_{2\mu}p_{4\nu}+p_{2\nu}p_{4\mu}+\frac{1}{2}q^2 g_{\mu\nu})\\ &= \frac{\epsilon^2 e^2 g_S^2}{(t-m_V^2)^2}\left[4(p_1\cdot p_2+p_2\cdot p_3)(p_1\cdot p_4+p_3\cdot p_4)+t(4m_\chi^2-t)\right]\\ &= \frac{64\pi^2\epsilon^2\alpha\alpha_S}{(t-m_V^2)^2}\left[(s-m_\chi^2-m_e^2)^2+t(s-m_e^2)\right], \end{aligned} \tag{2.15}$$

where $\alpha_S = g_S^2/4\pi$. Therefore the differential cross section takes the following form

$$\frac{d\sigma}{d\Omega^*} = \epsilon^2\alpha\alpha_S\frac{(s-m_\chi^2-m_e^2)^2+t(s-m_e^2)}{s(t-m_V^2)^2}. \tag{2.16}$$

The expressions (2.11) and (2.15) will later be used for the calculation of the event rate, through a DM-electron scattering, in a direct detection DM experiment (see Chapter 4).

Chapter 3

Particle fluxes from DM decays

In this chapter we would like to develop a DM model that we will later use in the calculation of the event rate, through the scattering of a dark particle χ with an electron of DM detector. The dark particle χ is assumed to be a decay product of a progenitor DM particle ψ. We assume that χ interacts with SM particles through the mediation of a dark photon that kinetically mixes with the photon, as described in the previous chapter. For simplicity, we hypothesise that the DM particle decays monochromatically in a two-body decay process, as follows

$$\psi \to \chi + \chi, \tag{3.1}$$

where ψ and χ have masses m_ψ and $m_\chi < m_\psi/2$ respectively. It will be further assumed that ψ constitutes a fraction ζ of the amount of the total DM density at the time the CMB was released, so that

$$\left.\frac{\rho_\psi}{\rho_{\mathrm{DM}}}\right|_{\mathrm{CMB}} \equiv \zeta \lesssim 1, \qquad \tau_\psi \gg t_{\mathrm{CMB}} \tag{3.2}$$

where τ_ψ is the decay time of the DM progenitor and t_{CMB} is the time the CMB is released. Because of the exponential decay of ψ into χ's, the energy density of ψ at cosmic time t will generally be given by

$$\rho_\psi(r,t) = \rho_{\mathrm{DM}}(r,t)\zeta e^{-t/\tau_\psi}, \tag{3.3}$$

where r is the coordinate position, which is relevant for non-isotropic local DM densities. Our aim is to calculate the flux of particles χ originating from DM decays both from our galaxy (galactic contribution) and from outside our galaxy (extragalactic contribution). Because of (3.1) and because DM is non-relativistic ($v \sim \mathcal{O}(10^{-3})$)

the energy spectrum is to a good approximation monochromatic;

$$\frac{dN_\chi}{dE} = \mathcal{N}\delta(E - E_{\text{in}}), \tag{3.4}$$

where $E_{\text{in}} \equiv m_\psi/2$ is the χ injection energy and $\mathcal{N}$ is a normalization factor specifying the χ-multiplicity of the final state

$$\int \frac{dN_\chi}{dE} dE = \mathcal{N}. \tag{3.5}$$

In our case $\mathcal{N} = 2$.

3.1 Galactic contribution

DM in our galaxy has a nearly spherical density distribution, which is commonly parametrized as a double power-law density profile, as discussed in Sec. 1.5. Therefore $\rho_{\text{DM}}(r, t)$ in (3.3) becomes a halo density distribution $\rho_{\text{halo}}(r)$, where r is the distance to the GC.[2] Therefore the energy density of ψ, for $t \approx t_0$, where t_0=13.7 Gyr, is the age of the Universe, will be given by

$$\rho_\psi(r) = \rho_{\text{halo}}(r)\zeta e^{-t_0/\tau_\psi}. \tag{3.6}$$

We use the galactic coordinate system to express the positions for galactic sources located at (s, b, ϕ). Here, s is the distance of the source to the Sun, b the galactic latitude, the angular distance of a source from the Galactic plane and ϕ the galactic longitude, the angular separation between the position of a source projected perpendicularly onto the galactic plane (see Fig. (3.1)). The galactic coordinate system is a heliocentric system and $b = 0$, $\phi = 0$ points towards the GC. With some simple trigonometric considerations one can express the distance r of the source to the GC as follows

$$r(s, \theta) = \sqrt{s^2 - 2sR_\odot \cos\theta + R_\odot^2}, \tag{3.7}$$

where $\cos\theta = \cos b \cos\phi$ and θ is the angle between the line connected to the GC and the line of sight.

We are interested in the flux of particles χ, resulting from DM decays of ψ, which is a quantity defined as the number of particles per unit time, area and solid angle. To obtain this qualitatively, we think of a source term that gives the amount of

---

[2] The time dependence t on the energy density drops out for flux sources within the Milky Way, as the time difference between the time of the decay and the time that χ is observed is significantly smaller than the age of the Universe t_0.

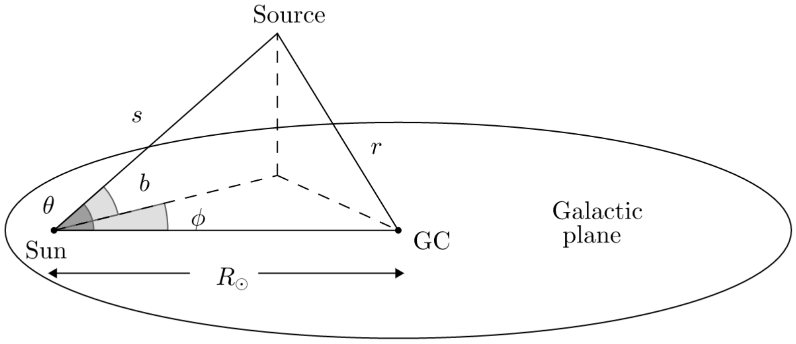

Figure 3.1: Graphical depiction of the Galactic plane. A source has galactic coordinates (s, b, ϕ) as viewed from Earth. r is the distance of a flux source to the GC. The θ angle spans between the line towards the GC and the line of sight s (darker shade).

particles per unit volume, time and energy,

$$\frac{dN(r)}{dt\,dV dE} = \frac{n_\psi(r)}{\tau_\psi}\frac{dN_\chi}{dE} = \frac{\rho_\psi(r)}{\tau_\psi m_\psi}\frac{dN_\chi}{dE}, \tag{3.8}$$

and integrate this over the "line of sight" (l.o.s.), which is the distance of the source to the detector, s. Therefore the averaged differential flux of particles χ per solid angle and energy can be written as

$$\frac{d\Phi_\chi}{d\Omega\, dE} = \frac{R_\odot}{4\pi}\frac{\rho_\odot}{m_\psi \tau_\psi}\frac{dN_\chi}{dE} J(\theta) \tag{3.9}$$

where $\rho_\odot$ and $R_\odot$ are the local DM density and the distance to the GC respectively, as defined in Sec. 1.5 and J is a dimensionless quantity, called the "J-factor", which is defined as [50]

$$J(\theta) = \int_{\text{l.o.s.}} \frac{ds}{R_\odot}\frac{\rho_\psi(r(s,\theta))}{\rho_\odot}. \tag{3.10}$$

The J-factor is replaced by the averaged J-factor, if one needs an integrated flux over a region $\Delta\Omega$, given either by the observational region of interest or the resolution of the telescope. If we consider a flux averaged over a spherical galactic halo, then the averaged J-factor will yield

$$\bar{J} = \frac{2\pi}{\Delta\Omega}\int d\theta \sin\theta\, J(\theta), \qquad \Delta\Omega = 2\pi \int_0^{\theta_{\max}} d\theta \sin\theta. \tag{3.11}$$

Because DM-detectors have no directional sensitivity, we calculate the full-sky flux with an acceptance region $0 < \theta < \pi$, so that by using the the NFW density profile (1.16), we obtain $\Delta\Omega = 4\pi$ and $\bar{J} = 2.84$. The differential particle flux per energy then yields

$$\begin{aligned}\frac{dJ_g}{dE} &= \frac{R_\odot}{4\pi}\frac{\rho_\odot}{m_\psi\tau_\psi}\frac{dN_\chi}{dE}\bar{J} && (3.12)\\ &= 1.1\times 10^4\,(\mathrm{cm}^2\,\mathrm{s}\,\mathrm{sr})^{-1}\zeta\left(\frac{100\,\mathrm{Gyr}}{\tau_\psi}\right)\left(\frac{100\,\mathrm{MeV}}{m_\psi}\right)\delta(E-E_{\mathrm{in}})e^{-\frac{13.8\,\mathrm{Gyr}}{\tau_\psi}} && (3.13)\end{aligned}$$

where we used the monochromatic spectrum defined in (3.4).

3.2 Extragalactic contribution

Extragalactic fluxes must take into account that the Universe expands while χ is traveling from its origin to Earth. We consider a monoenergetic source of decay with the energy E emitted at the cosmic time t and observed by our detector on Earth at t_0 with energy E_0. The extragalactic density is isotropic on large scales[3] so that, $\rho_\psi(r,t)\to\rho_\psi(t)$. The energy density scales with a^{-3}, hence

$$\rho_\psi(t) = \left(\frac{a_0}{a(t)}\right)^3 \Omega_{\mathrm{DM}}\rho_c\zeta e^{-t/\tau_\psi}, \tag{3.14}$$

where ρ_c and Ω_{DM} are today's critical energy density and density parameter respectively. The corresponding amount of particles produced per unit volume, time and energy for an extragalactic source is

$$\frac{dN_\chi(t)}{dt\,dV\,dE} = \frac{\rho_\psi(t)}{\tau_\psi m_\psi}\frac{dN_\chi}{dE} \tag{3.15}$$

This quantity is related to the differential luminosity density $d\mathcal{L}$, a quantity that describes the amount of energy emitted from a source per time and volume, as follow

$$\frac{d\mathcal{L}(t)}{dE} = \frac{\rho_\psi(t)}{\tau_\psi m_\psi}E\frac{dN_\chi}{dE} \tag{3.16}$$

The measured energy flux coming from one source with an absolute luminosity $L(t)$, is defined as the energy per time that has spread over a spherical shell area $A = 4\pi d_L^2$, where d_L is the luminosity distance. The differential energy flux of one source is thus given by

$$\frac{d\Phi_{\mathrm{s}}}{dE} = \frac{1}{4\pi d_L^2}\frac{dL}{dE}. \tag{3.17}$$

---

[3] It is a well known fact, that the Universe on smaller scales is anisotropic, which is one of the factors of structure formation. However on larger scales, the Universe is mostly isotropic.

The luminosity distance is defined as the proper distance of a source from the detector $r = a_0\chi$, times the shift in energy and time. Because of the Hubble expansion, the energy of the emitted particles decreases and the time interval between the arrival of consecutive particles increases. This relation yields

$$d_L^2 = a_0^2\chi^2 \frac{E}{E_0}\frac{\delta t_0}{\delta t}. \tag{3.18}$$

The physical distance that a particle with finite velocity v propagates, is given by the line element called the proper distance $dr = ad\chi = vdt$, where $d\chi$ is the comoving distance line element. Comoving variables have the Universe's expansion scaled out, meaning that a transformation $t \to t + \delta t$ leaves χ invariant. Therefore, the relation between the emitted and observed time interval is the following

$$\frac{\delta t}{\delta t_0} = \frac{a}{a_0}\frac{v_0}{v}. \tag{3.19}$$

A particle with momentum $p = \gamma mv = Ev$ at time t redshifts with a^{-1} and is observed at time t_0 with momentum $p_0 = E_0v_0$. Therefore the relation between emitted and observed energies is as follows

$$\frac{E}{E_0} = \frac{a_0}{a}\frac{v_0}{v}. \tag{3.20}$$

Using (1.6) and combining (3.19)-(3.20) the luminosity distance, in terms of redshift z, becomes $d_L^2 = a_0^2\chi^2(1+z)^2$. Since we are not measuring the flux coming from one source only, we may think that our detector is located at the centre of a spherical shell with volume dV, which is defined as the proper volume, so that a flux element in this shell is expressed as the proper number density of all flux sources (i.e. n_ψ), times the individual flux element of one source, times the proper volume element. The differential energy flux in this shell will then yield

$$\left.\frac{d\Phi}{dE}\right|_{\text{shell}} = \frac{n_\psi\, d\Phi_{\text{s}}}{dE}\, dV, \tag{3.21}$$

where the proper volume of a spherical element is given by $dV = 4\pi r^2 dr = 4\pi a^3\chi^2 d\chi$ and the number density n_ψ times the absolute luminosity will yield the luminosity density (3.16). To be able to compare with the galactic particle flux, we express the energy flux in terms of a differential particle flux, the amount of particles per time, surface area and energy. We are also interested in the differential flux in terms of observed energies E_0, instead of emitted $E(z)$. Finally the differential extragalactic (eg) particle flux is obtained by integrating over all shells

$$\left.\frac{dJ}{dE_0}\right|_{\text{shell}} \equiv \frac{1}{E_0}\left.\frac{d\Phi}{dE_0}\right|_{\text{shell}} \Rightarrow \frac{dJ_{\text{eg}}}{dE_0} = \int_{\text{shells}} \left.\frac{dJ}{dE_0}\right|_{\text{shell}} \tag{3.22}$$

Combining all equations (3.14)-(3.22), we obtain for the averaged differential eg particle flux

$$\frac{dJ_{\text{eg}}}{dE_0} = \frac{\Omega_{\text{DM}}\rho_c\zeta}{4\pi m_\psi \tau_\psi}\int_{z_0}^{z_{\text{dec}}} \frac{dz}{H(z)} e^{-t(z)/\tau_\psi} v(z)\frac{dN_\chi}{dE} \tag{3.23}$$

where $t(z)$ is given by equation (1.10). $v(z)$ is the velocity of the particle at the time of emission and is extracted from $ad\chi = vdt$, as discussed above. The conversion of dt to dz, obtained from (1.8), extracts the Hubble factor $H(z)$ in (3.23). One may solve the redshift integral analytically when the particle spectrum is monochromatic as in (3.4). The δ-function with an argument $f(y) = E(y) - E_{\text{in}}$ is expressed in terms of redshift $y = z + 1$, using the property of the δ-function,

$$\delta(f(y)) = \frac{\delta(y - y_0)}{|f'(y = y_0)|}. \tag{3.24}$$

From (3.20) the energy in terms of redshift is given by $E(y) = \sqrt{y^2 E_0^2 v_0^2 + m^2}$, from which follows for the energy spectrum

$$\frac{dN_\chi}{dE} = \frac{\mathcal{N}}{E_0 v_0 v_{\text{in}}}\delta\left(y - \frac{E_{\text{in}} v_{\text{in}}}{E_0 v_0}\right) \tag{3.25}$$

where v_{in} is the velocity of the particle associated with E_{in}. The differential eg particle flux can therefore be solved ($\mathcal{N} = 2$) giving

$$\begin{aligned}\frac{dJ_{\text{eg}}}{dE_0} &= \frac{J_0}{E_0 v_0}\int_1^{1+z_{\text{dec}}} dy \frac{e^{-t(y-1)/\tau_1}}{\sqrt{\kappa + y^3}}\frac{v}{v_{\text{in}}}\delta\left(y - \frac{E_{\text{in}} v_{\text{in}}}{E_0 v_0}\right)\\ &= J_0\left[\kappa\left(\frac{E_{\text{in}} v_{\text{in}}}{E_0 v_0}\right)^{-3} + 1\right]^{-\frac{1}{2}}\left(\frac{E_{\text{in}} v_{\text{in}}}{E_0 v_0}\right)^{-\frac{1}{2}} E_{\text{in}}^{-1} v_{\text{in}}^{-1} e^{-\alpha}\Theta(E_{\text{in}} - E_0)\end{aligned} \tag{3.26}$$

where $\kappa = \Omega_\Lambda/\Omega_m \simeq 2.24$ and the Heaviside Θ-function comes from conservation of energy. The constant J_0 carries the dimensions of the particle flux and it is given by

$$\begin{aligned}J_0 &= \frac{\Omega_{\text{DM}}\rho_c\zeta}{2\pi m_\psi \tau_\psi H_0\sqrt{\Omega_m}}\\ &\simeq 1.6 \times 10^4\,(\text{cm}^2\,\text{s}\,\text{sr})^{-1}\zeta\left(\frac{100\,\text{Gyr}}{\tau_\psi}\right)\left(\frac{100\,\text{MeV}}{m_\psi}\right).\end{aligned} \tag{3.27}$$

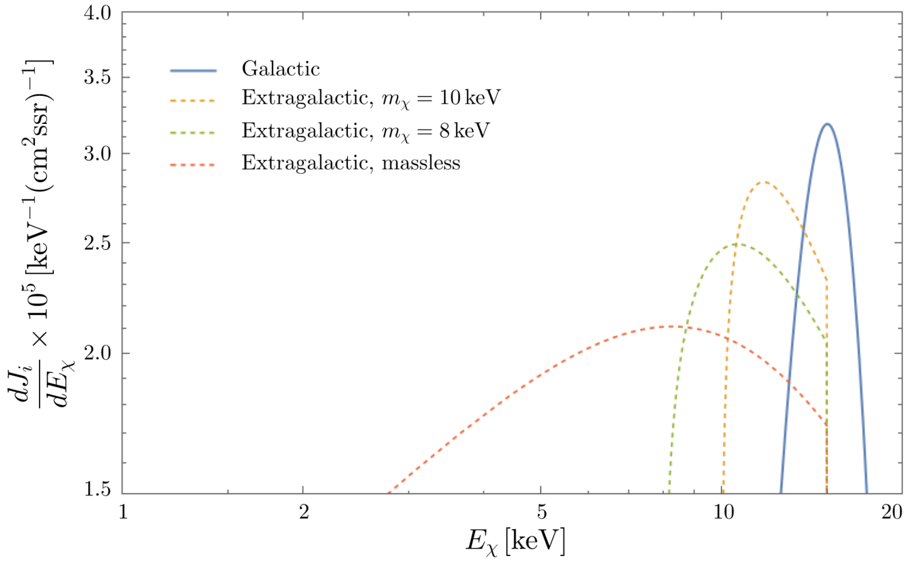

Figure 3.2: Combined plot of the Galactic (solid blue line) and Extragalactic (dashed lines) differential particle fluxes dJ_i/dE_χ as a function of particle energy E_χ. A Gaussian distribution function has been used to demonstrate the galactic particle flux. Because of this, the galactic flux in this example does not depend on the particle's mass m_χ, but rather on the deviation σ (here $\sigma = 2\,\mathrm{keV}$). In the case of the extragalactic flux, three examples have been used; particles with masses 10 keV (yellow), 8 keV (green) and a massless particle (red). In all cases a progenitor DM mass of $m_\psi = 30\,\mathrm{keV}$ and a decay time of $\tau_\psi = 100\,\mathrm{Gyr}$ is used.

Finally, the exponential factor in (3.26) with argument $\alpha = t\left(\frac{E_{\rm in}v_{\rm in}}{E_0 v_0} - 1\right)/\tau_\psi$ gives

$$e^{-\alpha} \simeq \left[\left(\frac{E_{\rm in}v_{\rm in}}{E_0 v_0}\right)^{-3/2}\left(\sqrt{\kappa + \left(\frac{E_{\rm in}v_{\rm in}}{E_0 v_0}\right)^3} + \sqrt{\kappa}\right)\right]^{-11.6\,\mathrm{Gyr}/\tau_\psi} . \tag{3.28}$$

As an exercise, we would like to see how the particle fluxes evolve with observed energy $E_0 = E_\chi$. To evaluate the galactic spectrum, we use a normal (Gaussian) distribution function, centred around an injection energy $E_{\rm in}$ and a standard deviation σ, as in

$$\frac{dN_\chi}{dE_\chi} = \frac{1}{\sqrt{2\pi\sigma^2}}\exp\left(-\frac{1}{2}\left(\frac{\mathrm{E}_\chi - \mathrm{E}_{\rm in}}{\sigma}\right)^2\right) . \tag{3.29}$$

The injection energy is in both cases given by $E_{\rm in} = m_\psi/2$, where for this specific example we use $m_\psi = 30\,\mathrm{keV}$ and a decay time of $\tau_\psi = 100\,\mathrm{Gyr}$. In the extragalactic particle flux case, we show three cases where the dark particle has masses $m_\chi =$ 10, 8 and 0 keV. These particle fluxes are plotted against the dark particle energy E_χ, as can be seen in Fig. (3.2).

Chapter 4

Direct detection searches from electron recoils

4.1 Introduction

When nuclear recoil energies fall below detection thresholds, event rates involving DM-electron recoils become important for light DM candidates, with masses in the keV to GeV range. The leading processes that involve low deposited energies in the detector are electron ionization, electron excitation, which involve DM-electron scattering, and molecular dissociation, which involves DM-nuclear scattering. These processes produce detectable signals in the form of individual electrons, photons, ions and phonons with typical energies in the eV range [51]. The ability to detect signals in these energy ranges are within reach with the current technological capabilities. The main challenge is to achieve a significant background discriminating ability to correctly identify events coming from known SM radiation (β-radiation, γ-rays etc.) from the ones coming from DM.

In this work, we focus on signals coming from individual electrons, which originate from inelastic DM-electron scattering processes causing atomic ionization,

$$\chi(E_\chi, \vec{p}_\chi) + \mathrm{Xe}(E_A) \rightarrow \chi(E'_\chi, \vec{p}^{\,'}_\chi) + \mathrm{Xe}^+(E'_A) + e^-(E'_e, \vec{p}^{\,'}_e), \tag{4.1}$$

where each particle's energy and momentum is ascribed in parenthesis. In this process an incoming DM particle χ with momentum $\vec{p}_\chi$ interacts with a xenon atom of atomic energy E_A, resulting in an outgoing DM with momentum $\vec{p}^{\,'}_\chi$, an excited xenon atom and an outgoing electron with momentum $\vec{p}^{\,'}_e$.

The first assumption in calculating the scattering event rate of this process is that DM interacts directly with electrons [51]-[52], so that if the interaction is independent of momentum transfer q, we can parametrize it by the total elastic cross section of the free electron-DM scattering, denoted as $\bar{\sigma}_e$, while the q-dependence of the interaction is carried by a DM form-factor, $F_{\rm DM}(q)$. The squared matrix element in this approach can therefore be parametrized as

$$\overline{|\mathcal{M}(q)|^2} = |\mathcal{M}(q = \alpha m_e)|^2 |F_{\rm DM}(q)|^2. \tag{4.2}$$

where $q = \alpha\, m_e$ is typical momentum scale for atomic processes. In this way, the determination of the differential cross-section and differential event rate follows by examining the individual ingredients in the next subsections.

4.2 The atomic form factor

A bound electron does not obey the free-particle energy-momentum relation, but has a fixed energy determined by the binding energy E_B^i of the atomic shell, given by $E_e = m_e - E_B^i$, where $i = nl$ denotes the orbital state defined by the quantum numbers n, the primary quantum number and l, the orbital quantum number. Energy conservation in this process implies $E_e' = m_e + E_d - E_B^i$, where $E_d = E_\chi - E_\chi'$ is the energy deposited in the detector. Since we are interested in the recoil energy of the electron, this relation reduces to $E_R = E_d - E_B^i$, where E_R is the recoil energy of the atomic electron.

The deposited energy can further be expressed in terms of the magnitude of the three-momentum transfer $q = |\vec{q}\,| = |\vec{p}_\chi - \vec{p}_\chi^{\,\prime}|$, the LAB frame DM velocity v and the scattering angle of the electron with respect to the incoming DM, θ_q, as follows

$$\begin{aligned} E_d &\approx \frac{p_\chi^2}{2m_\chi} - \frac{p_\chi'^2}{2m_\chi} = \frac{m_\chi\, v^2}{2} - \frac{|m_\chi\, \vec{v} - \vec{q}\,|^2}{2m_\chi} \\ &= \vec{v}\cdot\vec{q} - \frac{q^2}{2m_\chi} = vq\cos\theta_q - \frac{q^2}{2m_\chi}, \end{aligned} \tag{4.3}$$

where the process is taken to be non-relativistic. The kinematic requirement to overcome the electron's binding energy is that χ has an incoming velocity larger than a minimum velocity given by the following equation

$$v_{\rm min}(q) = \frac{E_d}{q} + \frac{q}{2m_\chi}, \tag{4.4}$$

which is a solution to equation (4.3) when $\vec{q}$ is antiparallel to $\vec{p}_\chi$, i.e. for $\theta_q = \pi$. For a fixed electron recoil energy, atomic binding energy and DM mass, this minimum velocity depends on the momentum transfer q, which can take any value, due to the uncertainty in the initial electron momentum p_e.

Since the bound electron does not carry a fixed momentum, the calculation of the interacting matrix element is slightly different than in the case of an unbound particle. Generally, this is determined by the S-matrix element obtained from the interacting Hamiltonian $H_{\text{int}}(\vec{r})$ of the process. For free propagating particles it is determined by using plane waves as incoming and outgoing particles (see (A.15)). However, since the initial electron momentum is not fixed, one can express it with a distribution function given by the Fourier transform of the bound state wave function, $\tilde{\Psi}_{nlm}(\vec{p}_e)$, corresponding to that shell. The outgoing electron is approximately given as a free plane wave with a wave function $\Psi_{\vec{p}_e'}(\vec{r}) = e^{i\vec{p}_e^{\,'}\cdot\vec{r}}$, which enters the matrix element as a Fourier transform in momentum space. Therefore the invariant matrix element for the process $p_\chi + p_e \to p_\chi' + p_e'$ is written as

$$\int \frac{d^3p_e}{(2\pi)^3}\frac{d^3p_e'}{(2\pi)^3}\tilde{\Psi}_{nlm}(\vec{p}_e)\tilde{\Psi}^*(\vec{p}_e^{\,'})\langle\vec{p}_\chi^{\,'},\vec{p}_e^{\,'}|H_{\text{int}}(\vec{r})|\vec{p}_\chi,\vec{p}_e\rangle. \tag{4.5}$$

Further, following the expression (A.15) by exchanging $\vec{p}_i$ with $\vec{q} = \vec{p}_\chi^{\,'} - \vec{p}_\chi$, since the momentum transfer is expressed in the kinematic requirement (4.4), one has

$$\begin{aligned}\int \frac{d^3p_e}{(2\pi)^3}\frac{d^3p_e'}{(2\pi)^3}\int d^3r\, e^{-i(\vec{p}_e^{\,'}-\vec{q}-\vec{p}_e)\cdot\vec{r}}\tilde{\Psi}_{nlm}(\vec{p}_e)\tilde{\Psi}^*(\vec{p}_e^{\,'})\mathcal{M}(\vec{q})\\ = \int \frac{d^3p_e}{(2\pi)^3}\tilde{\Psi}^*(\vec{q}+\vec{p}_e)\tilde{\Psi}_{nlm}(\vec{p}_e)\mathcal{M}(\vec{q}) \equiv f(\vec{q})\mathcal{M}(\vec{q}),\end{aligned} \tag{4.6}$$

where $f(\vec{q})$ is an atomic form factor, which is defined as

$$\begin{aligned}f(\vec{q}) &= \int \frac{d^3p_e}{(2\pi)^3}\tilde{\Psi}^*(\vec{q}+\vec{p}_e)\tilde{\Psi}_{nlm}(\vec{p}_e) = \int d^3r\Psi^*(\vec{r})\Psi_{nlm}(\vec{r})e^{i\vec{q}\cdot\vec{r}}\\ &= \int d^3r\Psi_{nlm}(\vec{r})e^{-i(\vec{p}_e^{\,'}-\vec{q})\cdot\vec{r}} = \tilde{\Psi}_{nlm}(\vec{p}_e^{\,'}-\vec{q}).\end{aligned} \tag{4.7}$$

where an outgoing particle wave $\Psi^*(\vec{r}) = e^{-i\vec{p}_e^{\,'}\cdot\vec{r}}$ has been used.

From what we obtained so far, one can write down a differential cross section following Appendices A.2 in an arbitrary system of reference. The flux factor in (A.13) is equivalently written as $F = 4E_1E_2|\vec{v}_1 - \vec{v}_2| \equiv 4E_1E_2v_{12}$, where v_{12} is the relative velocity between the two incoming particles. Since the form factor (4.7) depends on the quantum numbers nlm, the cross-section is different for different states of the atom, corresponding to these quantum numbers. Furthermore, the magnetic quantum number m, is not affecting the atomic electron's energy if there is no electromagnetic field present in the experiment. Since the LXe experiments do not apply strong enough electromagnetic fields, only the states nl are affected and thus a sum over all magnetic numbers m must be imposed

$$\begin{aligned} d\sigma^i v =& \frac{|\mathcal{M}(q=\alpha m_e)|^2}{4E_\chi\, E_e}\frac{d^3p'_e}{(2\pi)^3 2E'_e}\frac{d^3q}{(2\pi)^3 2E'_\chi}(2\pi)\delta(E_\mathrm{i}-E_\mathrm{f})|F_\mathrm{DM}(q)|^2 \\ &\times \sum_{m=-l}^{l} |\tilde{\Psi}_{nlm}(\vec{p}_e^{\,\prime}-\vec{q})|^2 \Theta(v-v_\mathrm{min}), \end{aligned} \tag{4.8}$$

where the function $\Theta(v - v_\mathrm{min})$ comes from the condition of minimum velocity to ionize an atomic electron. Since we are interested in a differential cross section with recoil energy dependence, we rewrite the outgoing momentum space element in terms of its recoil energy and the solid angle corresponding to the outgoing electron's momentum vector

$$\begin{aligned} d^3p'_e &= p_e'^2 dp'_e d\Omega_{p'_e} = p'_e E'_e dE'_e d\Omega_{p'_e} \\ &= p'_e E'_e E_R \, d\,\mathrm{ln} E_R \, d\Omega_{p'_e} \\ &\simeq \frac{1}{2} p_e'^3 d\,\mathrm{ln} E_R d\Omega_{p'_e} \end{aligned} \tag{4.9}$$

where in the last line, a non-relativistic approximation for the outgoing momentum is taken. Continuing in the non-relativistic regime we approximate $E_e \approx E'_e \approx m_e$ and $E_\chi \approx E'_\chi \approx m_\chi$ so that we write

$$\begin{aligned} \frac{d\sigma^i v}{d\mathrm{ln} E_R} =& \frac{|\mathcal{M}(q=\alpha m_e)|^2}{(16\pi)^2 m_\chi^2\, m_e^2} \int d^3q \int d\Omega_{p'_e} |F_\mathrm{DM}(q)|^2 \\ &\times \frac{2p_e'^3}{(2\pi)^3} \sum_{m=-l}^{l} |\tilde{\Psi}_{nlm}(\vec{p}_e^{\,\prime}-\vec{q})|^2 \delta(E_\mathrm{i}-E_\mathrm{f}) \Theta(v-v_{min}) \\ =& \frac{\bar{\sigma}_e}{16\pi\mu_{\chi e}^2} \int d^3q \, |F_\mathrm{DM}(\vec{q})|^2 |f_\mathrm{ion}^{nl}(p'_e, q)|^2 \delta(E_\mathrm{i}-E_\mathrm{f}) \Theta(v-v_{min}) \end{aligned} \tag{4.10}$$

where $\mu_{\chi e}$ is the reduced mass. $|f_\mathrm{ion}^{nl}(p'_e, q)|$ is the ionization form factor which describes the likelihood that an electron in the bound state nl will be ionized with outgoing momentum $p'_e \approx \sqrt{2E_R m_e}$ through a momentum transfer q, defined as

$$|f_\mathrm{ion}^{nl}(p'_e, q)|^2 = \frac{2p_e'^3}{(2\pi)^3} \int d\Omega_{p'_e} \sum_{m=-l}^{l} |\tilde{\Psi}_{nlm}(\vec{p}_e^{\,\prime}-\vec{q})|^2 \tag{4.11}$$

Further, the total elastic and non-relativistic fiducial cross section for a free DM-electron scattering is defined, following (A.17) by integration over the total angular region,

$$\bar{\sigma}_e \equiv \frac{\mu_{\chi e}^2 |\mathcal{M}(q = \alpha m_e)|^2}{16\pi m_\chi^2 m_e^2}, \tag{4.12}$$

where the non-relativistic condition $s = (E_1^* + E_2^*)^2 \simeq (m_1 + m_2)^2$ has been used. To evaluate the ionization form factor we use the fourier transformation of the wavefunction, decomposed into a momentum part $\chi_{nl}(p)$ and an angular part $Y_{lm}(\theta_p, \phi_p)$, which is a spherical harmonic with angles that refer to the momentum vector, as follows

$$\tilde{\Psi}_{nlm}(\vec{p}) = \chi_{nl}(p) Y_{lm}(\theta_p, \phi_p). \tag{4.13}$$

To calculate the radial component of the wave function, we multiply both sides with $Y_{lm}^*(\theta_p, \phi_p)$, sum over all angular variables m and use the addition theorem for spherical harmonics. The addition theorem states that for two unit vectors $\hat{x}$ and $\hat{y}$ with spherical coordinates (θ, ϕ) and (θ', ϕ') respectively, obey the following relation

$$P_l(\hat{x} \cdot \hat{y}) = \frac{4\pi}{2l+1} \sum_{m=-l}^{l} Y_{lm}(\theta, \phi) Y_{lm}^*(\theta', \phi'), \tag{4.14}$$

where P_l is the Legendre polynomial of degree l. If $\hat{x} = \hat{y}$ then $P_l(\hat{x} \cdot \hat{y}) = 1$. Therefore

$$\begin{aligned}
\chi_{nl}(p) &= \frac{4\pi}{2l+1} \sum_{m=-l}^{l} \tilde{\Psi}_{nlm}(\vec{p}) Y_{lm}^*(\theta_p, \phi_p) \\
&= \frac{4\pi}{2l+1} \sum_{m=-l}^{l} \int drr^2 R_{nl}(r) \int d\Omega\, Y_{lm}(\theta, \phi) Y_{lm}^*(\theta_p, \phi_p) e^{-i\vec{p}\cdot\vec{x}} \\
&= 2\pi(-1)^l \int drr^2 R_{nl}(r) \int d(\cos\theta_{pr}) P_l(\cos\theta_{pr}) e^{ipr\cos\theta_{pr}} \\
&= 4\pi i^l (-1)^l \int drr^2 R_{nl}(r) j_l(pr),
\end{aligned} \tag{4.15}$$

where on the third line we used $P_l(-\cos\theta) = (-1)^l P_l(\cos\theta)$ and change the integration variable. On the last line, Gegenbauer's formula [53] is being used, which relates the spherical Bessel functions with the integral over a Legendre polynomial of the same degree

$$j_n(z) = \frac{1}{2}(-i)^n \int_{-1}^{1} P_n(\cos\theta) e^{iz\cos\theta} d(\cos\theta). \tag{4.16}$$

Returning to the ionization form factor and using (4.14) for two equal unit vectors we obtain

$$\begin{aligned}
|f_{\text{ion}}^{nl}(p'_e,q)|^2 &= \frac{2p_e'^3}{(2\pi)^3}\frac{2l+1}{4\pi}\int d\Omega_{p'_e}|\chi_{nl}(|\vec{p}_e^{\,\prime}-\vec{q}|)|^2 \\
&= \frac{(2l+1)p_e'^3}{(2\pi)^3}\int_{-1}^{1} d(\cos\theta_{p'_e})|\chi_{nl}(|\vec{p}_e^{\,\prime}-\vec{q}|)|^2 \\
&= \frac{(2l+1)p_e'^2}{(2\pi)^3 q}\int_{|\vec{p}_e^{\,\prime}-\vec{q}|}^{|\vec{p}_e^{\,\prime}+\vec{q}|} dp_e\, p_e|\chi_{nl}(p_e)|^2, \qquad (4.17)
\end{aligned}$$

where the momentum transfer relation $\vec{p}_e = \vec{p}_e^{\,\prime} - \vec{q}$ is used to determine both the limits of the integration and to change the integration variable. Namely

$$\vec{p}_e^{\,2} = \vec{p}_e^{\,\prime 2} + \vec{q}^{\,2} - 2p'_e q\cos\theta_{p'_e} \Rightarrow -d(\cos\theta_{p'_e}) = \frac{p_e}{qp'_e}dp_e. \qquad (4.18)$$

Therefore (4.10) is written as

$$\frac{d\sigma^i v}{d\ln E_R} = \frac{\bar{\sigma}_e}{8\mu_{\chi e}^2}\int dq\, q^2\,|F_{\text{DM}}(q)|^2|f_{\text{ion}}^{nl}(p'_e,q)|^2\int_{-1}^{1} d\cos\theta_q\delta(E_{\text{i}}-E_{\text{f}})\Theta(v-v_{\text{min}}) \quad (4.19)$$

where the energy conserving delta function imposes $E_{\text{i}} - E_{\text{f}} = E_R + E_B - E_d$. Using E_d from Eq. (4.3), the argument in the delta-function becomes a function of $\cos\theta_q$, which can be simplified using the delta identity $\delta(f(\cos\theta_q))$ with $f(\cos\theta_q) = E_R + E_B + \frac{q^2}{2m_\chi} + vq\cos\theta_q$ that yields

$$\delta(f(\cos\theta_q)) = \frac{\delta(\cos\theta_q - \cos\theta_{q0})}{vq}. \qquad (4.20)$$

This makes the integration over $\cos\theta_q$ trivial, yielding a differential cross-section

$$\frac{d\sigma^i v}{d\ln E_R} = \frac{\bar{\sigma}_e}{8\mu_{\chi e}^2}\int dq\, q\,|F_{\text{DM}}(q)|^2|f_{\text{ion}}^{nl}(p'_e,q)|^2\Theta(v-v_{\text{min}}). \qquad (4.21)$$

4.3 Velocity distribution

Since the DM velocity v cannot take arbitrary values, one takes a velocity-averaged cross section over a DM velocity distribution, as described in Sec. 1.5. For simplicity, we assume an ideal DM gas that is isothermal and isotropic and obeys a Maxwell-

Boltzmann velocity distribution, which in the LAB frame is given by

$$f(\vec{v}+\vec{v}_{\mathrm{E}}) = \frac{1}{N_{\mathrm{esc}}}\exp\left(-\frac{(\vec{v}+\vec{v}_E)^2}{v_0^2}\right), \tag{4.22}$$

where $\vec{v}_{\mathrm{E}}$ is the velocity of the Earth relative to the dark matter halo distribution, v_0 is a characteristic velocity of the distribution and N_{esc} is the normalization constant defined in Eq. (1.18). Thus the thermally averaged cross-section is given by

$$\begin{aligned} \frac{d\langle\sigma^i v\rangle}{d\mathrm{ln}E_R} &= \int d^3v f(\vec{v},\vec{v}_{\mathrm{E}})\frac{d\sigma^i v}{d\mathrm{ln}E_R} \\ &= \frac{\bar{\sigma}_e}{8\mu_{\chi e}^2}\int dq\, q\, |F_{\mathrm{DM}}(\vec{q})|^2 |f_{\mathrm{ion}}^{nl}(p_e', q)|^2 \eta(v_{\mathrm{min}}), \end{aligned} \tag{4.23}$$

where $\eta(v_{\mathrm{min}}) \equiv \langle \frac{1}{v}\Theta(v - v_{\mathrm{min}})\rangle$, which corresponds to the DM velocity distribution in the target frame of the detector. The distribution itself may run through all the velocity space, however a maximum velocity v_{max} determined by the escape velocity v_{esc} sets the upper boundary to the velocity integral. The velocity distribution will thus be

$$\begin{aligned} \eta(v_{\mathrm{min}}) &= \int d^3v \frac{1}{v} f(\vec{v},\vec{v}_{\mathrm{E}})\Theta(v - v_{\mathrm{min}}) \\ &= \int_0^{2\pi} d\phi \int_{-1}^{1} d(\cos\theta) \int_{v_{\mathrm{min}}}^{v_{\mathrm{max}}} dv\, v f(\vec{v},\vec{v}_{\mathrm{E}}), \end{aligned} \tag{4.24}$$

where the maximum velocity is related to the escape velocity as

$$|\vec{v}+\vec{v}_{\mathrm{E}}| \leq v_{\mathrm{esc}}, \tag{4.25}$$

which yields a maximum DM velocity

$$v_{\mathrm{max}}(\theta) = \sqrt{v_{\mathrm{esc}}^2 - v_{\mathrm{E}}^2(1-\cos\theta^2)} - v_{\mathrm{E}}\cos\theta, \tag{4.26}$$

where θ is the scattering angle in the galactic rest frame. Therefore, the upper boundary runs in the range $v_{\mathrm{esc}} - v_{\mathrm{E}} \leq v_{\mathrm{max}}(\theta) \leq v_{\mathrm{esc}} + v_{\mathrm{E}}$. Since the integration over θ is simpler, one may change the integration order, which will yield an upper boundary for $\cos\theta$ for a given velocity v, as follows

$$\cos\theta_{\mathrm{max}}(v) = \frac{v_{\mathrm{esc}}^2 - v^2 - v_{\mathrm{E}}^2}{2vv_{\mathrm{E}}}, \tag{4.27}$$

so that for a maximum value of $\cos\theta$, this corresponds to $v = v_{\mathrm{esc}} - v_{\mathrm{E}}$. Therefore, we can split the velocity integral, where for values $v_{\mathrm{min}} \leq v \leq v_{\mathrm{esc}} - v_{\mathrm{E}}$ the upper boundary of the angular integral takes the maximum value and for values $v_{\rm esc}-v_{\rm E} \leq v \leq v_{\rm esc}+v_{\rm E}$ the upper boundary of the angular integral gets the value set by (4.27)

$$\eta(v_{\rm min}) = 2\pi\left(\int_{v_{\rm min}}^{v_{\rm esc}-v_{\rm E}} vdv \int_{-1}^{1} d(\cos\theta) + \int_{v_{\rm esc}-v_{\rm E}}^{v_{\rm esc}+v_{\rm E}} vdv \int_{-1}^{\cos\theta_{\rm max}(v)} d(\cos\theta)\right) f(\vec{v},\vec{v}_{\rm E}), \tag{4.28}$$

which yields following result

$$\eta(v_{\rm min}) = \frac{2\pi v_0^2}{N_{\rm esc}}\left[\frac{\sqrt{\pi}}{4}\frac{v_0}{v_{\rm E}}\left(\mathrm{erf}\left(\frac{v_{\rm E}-v_{\rm min}}{v_0}\right)+\mathrm{erf}\left(\frac{v_{\rm E}+v_{\rm min}}{v_0}\right)\right)-e^{-\frac{v_{\rm esc}^2}{v_0^2}}\right] \equiv \eta_1. \tag{4.29}$$

However one may notice that this formula holds only for $v_{\rm min} \leq v_{\rm esc}-v_{\rm E}$, since for values $v_{\rm min} \geq v_{\rm esc}-v_{\rm E}$ it yields negative results and thus gives raise to unphysical differential rates. Therefore a separate distribution is needed for the range $v_{\rm esc}-v_{\rm E} \leq v_{\rm min} \leq v_{\rm esc}+v_{\rm E}$, which is given by the following integral

$$\eta(v_{\rm min}) = 2\pi\int_{v_{\rm min}}^{v_{\rm esc}+v_{\rm E}} vdv \int_{-1}^{\cos\theta_{\rm max}(v)} d(\cos\theta) f(\vec{v},\vec{v}_{\rm E}), \tag{4.30}$$

yielding

$$\eta(v_{\rm min}) = \frac{2\pi v_0^2}{N_{\rm esc}}\left[\frac{\sqrt{\pi}}{4}\frac{v_0}{v_{\rm E}}\left(\mathrm{erf}\left(\frac{v_{\rm E}-v_{\rm min}}{v_0}\right)+\mathrm{erf}\left(\frac{v_{\rm esc}}{v_0}\right)\right)-\frac{(v_{\rm E}+v_{\rm esc}-v_{\rm min})}{2v_{\rm E}}e^{-\frac{v_{\rm esc}^2}{v_0^2}}\right] \equiv \eta_2. \tag{4.31}$$

Finally for values in the range $v_{\rm min} \geq v_{\rm esc}+v_{\rm E}$ there should be no contribution to the differential rate. Summarizing, the final averaged transverse velocity takes the following form

$$\eta(v_{\rm min}) = \eta_1\Theta(v_{\rm esc}-v_{\rm E}-v_{\rm min}) + \eta_2\Theta(v_{\rm esc}+v_E-v_{\rm min})\Theta(v_{\rm min}-v_{\rm esc}+v_{\rm E}). \tag{4.32}$$

4.4 RHF wave functions

The Hartree-Fock (HF) method is a method used to deal with a many-body system in a stationary state, by using approximation methods to determine the wave function and the energy of such a system. If the system in question is fermionic, then a Slater determinant is an approximation to its wave function. This ensures that the system satisfies anti-symmetry requirements and thus the Pauli principle is obeyed.

More accurate methods in approximating N-body wave functions has since been developed. The foundations of such a development were laid out by Clemens C. J. Roothaan [54] and thus the method was named the Roothaan-Hartree-Fock (RHF) method. Clementi and Roetti [55] were the first to produce comprehensive tables of RHF wave functions, which were later improved by C. F. Bunge *et al.*, 1993 [56]. According to [56], RHF atomic wave functions are approximations to conventional HF wave functions in which the radial atomic orbitals R_{nl} are expanded as a finite superposition of primitive radial functions

$$R_{nl}(r) = \sum_j C_{jnl}\, S_{jl}(r), \tag{4.33}$$

where C_{jnl} are the basis coefficients and S_{jl} is a set of Slater-type orbital (STO) functions given by

$$S_{jl}(r) = N_{jl}\, a_0^{-3/2} \left(\frac{r}{a_0}\right)^{n_{jl}-1} e^{-Z_{jl} r/a_0}, \tag{4.34}$$

where a_0 is the Bohr radius[4], n_{jl} is the principle quantum number and Z_{jl} the orbital exponent both corresponding to the orbital quantum number l. N_{jl} is a normalization factor given by

$$N_{jl} = \frac{(2Z_{jl})^{n_{jl}+1/2}}{\sqrt{(2n_{jl})!}}. \tag{4.35}$$

Eq. (4.15) can be evaluated analytically with the following result,

$$\begin{aligned}
\chi_{nl}(p) &= 4\pi\, i^l (-1)^l \sum_j C_{jnl} N_{jl} a_0^{-n_{jl}-1/2} \int_0^\infty dr r^{n_{jl}+1} e^{-Z_{jl} r/a_0} j_l(pr) \\
&= (-1)^l \sum_j C_{jnl} \frac{2^{-l+n_{jl}}}{\sqrt{(2n_{jl})!}} \left(\frac{2\pi a_0}{Z_{jl}}\right)^{\frac{3}{2}} \left(\frac{ipa_0}{Z_{jl}}\right)^l \frac{\Gamma(2+l+n_{jl})}{\Gamma(3/2+l)} \\
&\quad \times {}_2F_1\left[\frac{1}{2}(2+n_{jl}+l), \frac{1}{2}(3+n_{jl}+l), \frac{3}{2}+l, -\left(\frac{pa_0}{Z_{jl}}\right)^2\right]
\end{aligned} \tag{4.36}$$

where ${}_2F_1[a,b,c,z]$ is a Gaussian hypergeometric function defined by the following power series

$${}_2F_1[a,b,c,z] = \sum_{n=0}^{\infty} \frac{(a)_n (b)_n}{(c)_n} \frac{z^n}{n!} \tag{4.37}$$

where $(a)_n = \Gamma(a+n)/\Gamma(a)$ is the Pocchhammer symbol.

The numerical values of orbital energies, coefficients C_{jnl} and exponents Z_{jl} of a

---

[4] Here the Bohr radius is $a_0 = 0.268\,\mathrm{keV}^{-1}$. Therefore the radial wave function component has the dimensions $[\chi_{nl}] = \mathrm{keV}^{-3/2}$, which makes f_{ion} (4.17) dimensionless.

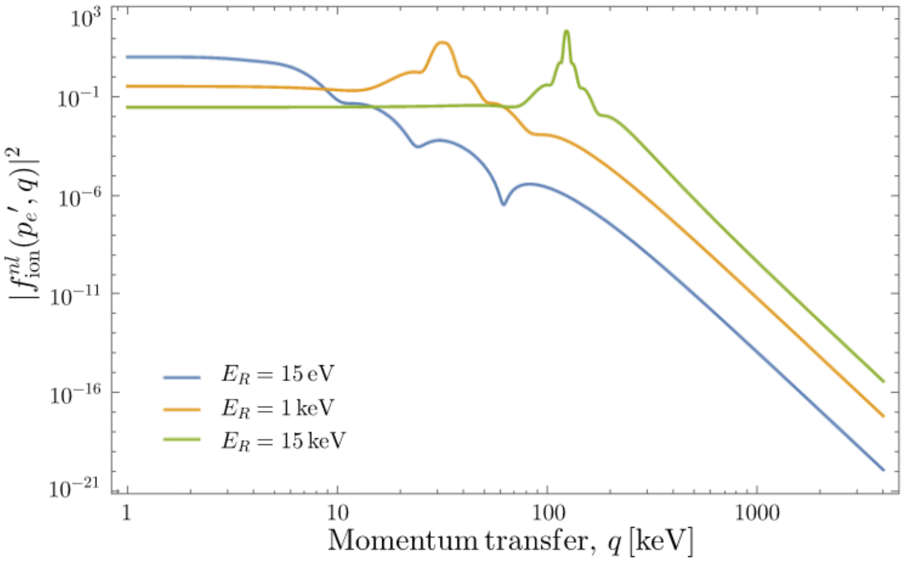

Figure 4.1: Ionization form factor for the 5p shell electron for three different electron recoil energies as indicated in the legends.

given element with atomic numbers Z=2-54 can be read off [56]. These values for all orbital states of ^{54}Xe are listed in Tables 4.1[5]. As an example the ionization form factor (4.17), for the state 5p is shown in Fig. (4.1) for three different electron recoil energies E_R = 15 eV, 1 keV and 15 keV. We observe that the ionization form factor is suppressed at higher transfer momenta and higher recoil energies peak at higher transfer momenta.

---

[5] The energies are initially given in a.u.(M), where 1 a.u.=27.2113961 eV and 1 a.u.(M)=1 a.u.$\times(1 + m/M)^{-1}$, where m is the electron mass and M the nuclear mass. The mass number for Xe is 131.293 u, therefore the nuclear mass is $M \approx 131.293 \times 938\,\rm MeV\ =\ 1.232 \times 10^{8}\,eV$, giving a correction factor to the RHF energy 0.999996.

State	$1s$	$2s$	$3s$	$4s$	$5s$
E [eV]	33317.56	5152.20	1093.235	213.7797	25.6985
State		$2p$	$3p$	$4p$	$5p$
E [eV]		4837.7072	958.43	163.494	12.4433
State			$3d$	$4d$	
E [eV]			710.728	75.5894	

$n_{j0}0$	Z_{j0}	C_{j10}	C_{j20}	C_{j30}	C_{j40}	C_{j50}
1S	54.9179	-0.965401	0.313912	-0.140382	0.064020	-0.022510
2S	47.2500	-0.04035	0.236118	-0.125401	0.059550	-0.021077
2S	26.0942	0.00189	-0.985333	0.528161	-0.251138	0.088978
3S	68.1771	-0.003868	0.000229	-0.000435	0.000152	-0.000081
3S	16.8296	-0.000263	-0.346825	0.494492	-0.252274	0.095199
3S	12.0759	0.000547	0.345786	-1.855445	1.063559	-0.398492
4S	31.9030	-0.000791	-0.120941	0.128637	-0.071737	0.025623
4S	8.0145	0.000014	-0.005057	-0.017980	-0.563072	0.274471
4S	5.8396	-0.000013	0.001528	0.000792	-0.697466	0.291110
5S	14.7123	-0.000286	-0.000286	0.333907	-0.058009	0.011171
5S	3.8555	0.000005	-0.000281	-0.000228	-0.018353	-0.463123
5S	2.6343	-0.000003	0.000134	0.000191	0.002292	-0.545266
5S	1.8124	0.000001	-0.00004	-0.000037	-0.000834	-0.167779
$n_{j1}1$	Z_{j1}	C_{j21}	C_{j31}	C_{j41}	C_{j51}	
1S	58.7712	0.051242	0.000264	0.013769	-0.005879	
2S	22.6065	0.78107	0.622357	-0.426955	0.149040	
2S	48.9702	0.11491	-0.009861	0.045088	-0.018716	
3S	13.4997	-0.000731	-0.952677	0.748434	-0.266839	
3S	9.8328	0.000458	-0.3379	0.132850	-0.031096	
3S	40.2591	0.083993	-0.02634	0.059406	-0.024100	
4S	7.1841	-0.000265	-0.000384	-0.679569	0.267374	
4S	5.1284	0.000034	-0.001665	-0.503653	0.161460	
4S	21.5330	0.009061	0.087491	-0.149635	0.059721	
5S	3.4469	-0.000014	0.00024	-0.014193	-0.428353	
5S	2.2384	0.000006	-0.000083	0.000528	-0.542284	
5S	1.4588	-0.000221	0.000026	-0.000221	-0.201667	
$n_{j2}2$	Z_{j2}	C_{j32}	C_{j42}			
3D	19.9787	0.220185	-0.013758			
3D	12.2129	0.603140	-0.804573			
3D	8.6994	0.194682	0.260624			
4D	27.7398	-0.014369	0.007490			
4D	15.9410	0.049865	0.244109			
4D	6.0580	-0.000300	0.597018			
4D	4.0990	0.000418	0.395554			

Table 4.1: Orbital energies for all the electron states given in eV (above). C_{jnl} and Z_{jl} values for all the electron states of ^{54}Xe (bellow). The values of this table are taken from [56].

4.5 Sommerfeld enhancement

As seen in the previous section, the ionization form factor, which is a consequence of the presence of a binding potential, acts as a suppression factor for large momentum transfer in the cross-section. However, an opposite effect is observed, that acts as an enhancement to the cross-section similar to what has been discussed in Sec. 2.1. In this case the escaping electron is affected by the attractive potential around the nucleus, yielding an enhancement factor, called the Fermi factor, which gives the ratio between the exact wavefunction and the free wavefunction at origin [51]. Following [38] it can be shown by solving the Schrödinger equation for a Coulomb potential of an attractive nucleus,

$$S(p'_\mathrm{e}) = \frac{|\Psi_\mathrm{exact}(0)|^2}{|\Psi_\mathrm{free}(0)|^2} = \frac{2\pi\eta}{1-e^{-2\pi\eta}}, \qquad \eta = Z_\mathrm{eff}\frac{\alpha m_\mathrm{e}}{p'_\mathrm{e}} \tag{4.38}$$

where Z_eff is the effective charge felt by the escaping electron. In the following we will, for simplicity, take $Z_\mathrm{eff} \approx 1$.

4.6 Elastic cross-section and F_DM: non-relativistic case

To obtain the non-relativistic total cross-section, $\bar{\sigma}_e$, for a fixed momentum transfer $|\vec{q}| = \alpha m_e$ and a CMS energy $s = (E^*_\chi + E^*_e)^2$, we use non-relativistic expressions for CMS energies, comprised of a potential and a kinetic term

$$\begin{aligned} E^*_\chi &= m_\chi + \frac{1}{2} m_\chi v_\chi^2, \\ E^*_e &= m_e + \frac{1}{2} m_e v_e^2, \end{aligned} \tag{4.39}$$

where $v_\chi \sim 10^{-3} \ll 1$. Therefore the squared matrix element for a fermionic DM-electron scattering (2.10) can be expanded for small velocities as follows

$$\overline{|\mathcal{M}|^2} = 32\pi^2\epsilon^2\alpha\alpha_D \left[\frac{8m_\chi^2 m_e^2 + 2\alpha^2 m_e^2 (m_\chi^2 + m_e^2)^2 + \alpha^4 m_e^4}{(\alpha^2 m_e^2 + m_V^2)^2}\right] + \mathcal{O}(v^2). \tag{4.40}$$

Because of the small value of α, the expression (4.40) can be further simplified, by ignoring the terms $\mathcal{O}(\alpha^2)$ in the numerator, therefore yielding

$$\overline{|\mathcal{M}|^2} \simeq \frac{(16\pi)^2\epsilon^2\alpha\alpha_D m_\chi^2 m_e^2}{(\alpha^2 m_e^2 + m_V^2)^2}. \tag{4.41}$$

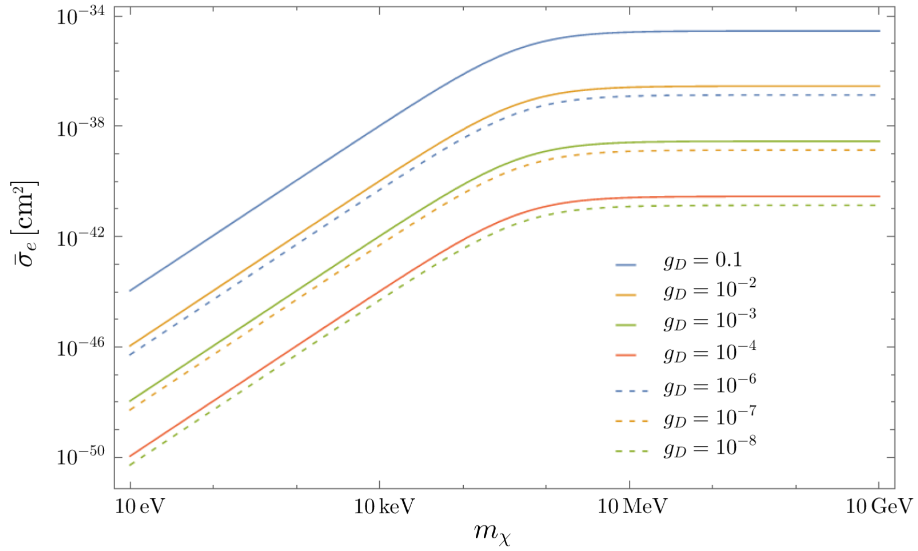

Figure 4.2: $\bar{\sigma}_e$-m_χ plane for two classes of models. One that has a heavy mediator with $F_{\mathrm{DM}} = 1$ (solid lines) and one with a light mediator with $F_{\mathrm{DM}} = \alpha^2 m_e^2/q^2$ (dashed lines). In the first case a mediator with a mass $m_V = 8$ MeV and a kinetic mixing of $\epsilon = 2\times 10^{-3}$ has been used. In the second case a mediator mass $m_V \sim$ meV is assumed and a kinetic mixing $\epsilon = 3\times 10^{-6}$. The dark sector couplings g_D are indicated in the legends.

The final expression is then obtained using (4.12). Two cases can further be observed regarding the relative mass of the mediator, one with a heavy ($m_V \gg \alpha m_e$) and one with a light mediator ($m_V \ll \alpha m_e$), namely

$$\bar{\sigma}_e = \frac{16\pi\mu_{\chi e}^2\epsilon^2\alpha\alpha_D}{(\alpha^2 m_e^2 + m_V^2)^2} \simeq \begin{cases} \dfrac{16\pi\mu_{\chi e}^2\epsilon^2\alpha\alpha_D}{m_V^4} & m_V \gg \alpha m_e \\ \dfrac{16\pi\mu_{\chi e}^2\epsilon^2\alpha\alpha_D}{(\alpha m_e)^4} & m_V \ll \alpha m_e \end{cases} \tag{4.42}$$

Fig. (4.2) shows the $\bar{\sigma}_e$-m_χ plane for those two classes of models; one with a heavy mediator with mass $m_V = 8$ MeV (solid lines) and one with a light mediator with mass $m_V \sim$ meV (dashed lines) for selected values of couplings g_D as is indicated in the legends. We observe that $\bar{\sigma}_e$ remains constant for $m_\chi \gtrsim m_e$ and starts decreasing when $m_\chi \sim m_e$.

F_{DM} follows from (4.2) for a given scattering process. For a fermionic dark particle-electron scattering, we use the results for the squared matrix element obtained in Sec. 2, Eq. (2.10), from which we obtain

$$\begin{aligned}|F_{\mathrm{DM}}(q)|^2 &= \frac{|\mathcal{M}(q)|^2}{|\mathcal{M}(q=\alpha\, m_e)|^2} \\ &= \left[\frac{2(s-m_\chi^2-m_e^2)^2-2sq^2+q^4}{2(s-m_\chi^2-m_e^2)^2-2s\alpha^2m_e^2+\alpha^4m_e^4}\right]\frac{(m_V^2+\alpha^2m_e^2)^2}{(m_V^2+q^2)^2}, \end{aligned} \tag{4.43}$$

where the term in squared brackets for non-relativistic velocities and small α-terms is approximately 1. Therefore the DM form factor can be written in the following form,

$$|F_{\mathrm{DM}}(q)| = \frac{m_V^2+\alpha^2m_e^2}{m_V^2+q^2} \simeq \begin{cases} 1 & m_V \gg \alpha m_e \\ \dfrac{\alpha^2m_e^2}{q^2} & m_V \ll \alpha m_e \end{cases} \tag{4.44}$$

4.7 Event rates

Summarizing, the thermally averaged differential cross-section times the Sommerfeld enhancement S yields

$$\frac{d\langle\sigma^i v\rangle}{d\ln E_R} = \frac{\bar{\sigma}_e}{8\mu_{\chi e}^2}\int_{q_{\min}}^{\infty} dq\, q\,\eta(v_{\min})\,|F_{\mathrm{DM}}(q)|^2|f_{\mathrm{ion}}^{nl}(p_{\mathrm{e}}', q)|^2 S(p_{\mathrm{e}}'), \tag{4.45}$$

where $q_{\min}$ is an small (but non-zero) momentum transfer[6]. The differential event rate is finally obtained by summing over all orbital states $i = nl$ in the differential velocity averaged cross-section, times the number of target nuclei per unit detector mass, times the number density of the dark matter source,

$$\frac{dR_{\mathrm{ion}}}{d\ln E_R} = N_T\frac{\rho_\chi}{m_\chi}\sum_i \frac{d\langle\sigma^i v\rangle}{d\ln E_R}, \tag{4.46}$$

where $N_T = \frac{N_0}{A}$ is the number of target nuclei per unit mass (with the Avogadro constant $N_0 = 6.02214\times10^{26}\,\mathrm{kg}^{-1}$), A is the mass-number of the target material (for Xe, $A = 131.293$) and $\rho_\chi = \rho_\odot$ is the local DM density.

Lastly, we evaluate this formula for various values of m_χ and a dark photon mass $m_V = 8$ MeV, which corresponds to $F_{\mathrm{DM}} = 1$. In order to cross-check our results with the literature, we use a total elastic cross section of $\bar{\sigma}_e = 10^{-37}\,\mathrm{cm}^2$ with a coupling $g_D = 10^{-2}$ and a kinetic mixing $\epsilon = 2\times10^{-3}$ appropriate for DM masses $m_\chi = \mathcal{O}(\mathrm{MeV})$, as shown in Fig. (4.2). The results of this evaluation can be seen

---

[6] In the non-relativistic approximation, a zero momentum transfer is not physical, as can be seen by (4.4)

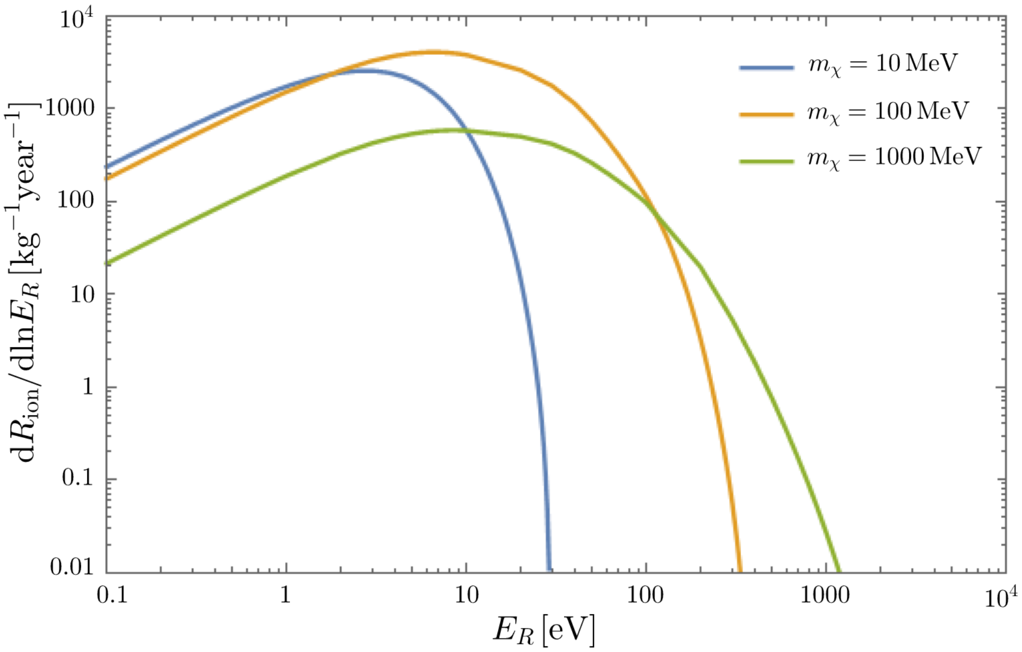

Figure 4.3: Differential event rates for DM masses of 10, 100 and 1000 MeV as indicated in the legends. A dark photon mass of m_V=8 MeV is used in all cases, which yields $F_{\text{DM}} = 1$. These results agree with [51] and [57].

in Fig. (4.3) for DM masses of 10, 100 and 1000 MeV. We observe that the event rates are at electron recoil energies in the eV energy range up to 1 keV. These results agree with [51] and [57].

Chapter 5

Atomic electron recoils from a cosmological relativistic background

5.1 Introduction

In this section, we would like to study the model developed in chapter 3, where a DM particle ψ decays into two lighter dark particles, such as in the decay process (3.1). Therefore, we utilize the galactic and extragalactic fluxes, which have been calculated in Sec. 3.1 and 3.2, to construct a differential event rate for direct DM detection.

We approach the problem similarly to what has been developed in the previous sections, but treat χ relativistically. When q is not dramatically different from the values considered in the previous sections, the definition of the ionization form factor as in (4.11) is still valid, as is the approach of parametrizing the squared matrix element into a q-dependent and q-independent part as in (4.2). The q-independent squared matrix element corresponds to an elastic scattering cross-section between a free electron and a dark particle, similar to what has been calculated in Sec. 4.6. In this approximation, however, we would like to see how the energy of the dark particle E_χ affects the total elastic cross-section, the DM form factor as well as the structure of the differential cross-section and event rate.

5.2 Elastic cross-section and F_{DM}: relativistic case

Because of the assumed relativistic nature of the dark particle χ, the energy dependence on the squared matrix element (4.2) needs to be explicitly carried along in the calculation of the event rate. The total squared matrix element can therefore be redefined to carry the energy dependence only in $F_{\rm DM}$ as follows

$$\overline{|\mathcal{M}(q,E_\chi)|^2} = \overline{|\mathcal{M}(q=\alpha\, m_e)|^2}\Big|_{v_\chi\to 0} |F_{\rm DM}(q,E_\chi)|^2, \tag{5.1}$$

from which the definition of the total elastic cross-section (4.42) can be recovered. $F_{\rm DM}$ for a fermionic χ can be derived using (2.10)

$$|F^f_{\rm DM}(q,E_\chi)|^2 = \left[\frac{2(s-m_\chi^2-m_e^2)^2-2sq^2+q^4}{8m_\chi^2m_e^2+\mathcal{O}(\alpha^2)}\right]\frac{(m_V^2+\alpha^2m_e^2)^2}{(m_V^2+q^2)^2}, \tag{5.2}$$

while for a scalar χ using (2.15) it yields

$$|F^S_{\rm DM}(q,E_\chi)|^2 = \left[\frac{(s-m_\chi^2-m_e^2)^2-q^2(s-m_e^2)}{4m_\chi^2m_e^2+\mathcal{O}(\alpha^2)}\right]\frac{(m_V^2+\alpha^2m_e^2)^2}{(m_V^2+q^2)^2}. \tag{5.3}$$

In a frame where the electron is non-relativistic with an energy $E_e \simeq m_e$, $s = (E_\chi+E_e)^2-(\vec{p}_\chi+\vec{p}_e)^2$ can be approximated as $s\simeq m_\chi^2+2E_\chi m_e+m_e^2$. This yields the following $F_{\rm DM}$ for a fermionic χ

$$|F^f_{\rm DM}(q,E_\chi)|^2 = \left[\frac{E_\chi^2}{m_\chi^2}-\frac{q^2(m_\chi^2+2E_\chi m_e+m_e^2)}{4m_\chi^2m_e^2}+\frac{q^4}{8m_\chi^2m_e^2}\right]\frac{(m_V^2+\alpha^2m_e^2)^2}{(m_V^2+q^2)^2}, \tag{5.4}$$

and for a scalar

$$|F^S_{\rm DM}(q,E_\chi)|^2 = \left[\frac{E_\chi^2}{m_\chi^2}-\frac{q^2(m_\chi^2+2E_\chi m_e)}{2m_\chi^2m_e^2}\right]\frac{(m_V^2+\alpha^2m_e^2)^2}{(m_V^2+q^2)^2}. \tag{5.5}$$

The upper and lower bounds of the physical region in t, yield the upper and lower bounds in $q^2=-t$, which have been obtained in (2.13). Using the non-relativistic electron approximation in s, as it is laid out above, we obtain the upper bound of the momentum transfer

$$q^2_{\rm max} = \frac{4(E_\chi^2-m_\chi^2)m_e^2}{m_\chi^2+2E_\chi m_e+m_e^2}. \tag{5.6}$$

This is imposed in (5.4) by multiplying with the heaviside function $\Theta(q_{\rm max}-q)$. Using the approach (5.4) for $F_{\rm DM}$ makes sense for relativistic particles. For non-relativistic particles $F_{\rm DM}\approx 1$, which is the approximation taken in Sec. 4.6, Eq. (4.44).

5.3 Event rates

To find an equivalent expression for the differential cross-section of the direct detection process, we go back to the expression for $d\sigma^i v$ (4.8), while using $d^3p'_e$ as in (4.9) and $|f^{nl}_{\text{ion}}(p'_e, q)|$ as in (4.11). We obtain

$$\frac{d\sigma^i v}{d\ln E_R} = \frac{\overline{|\mathcal{M}|^2}}{(16\pi)^2 m_e^2 E_\chi E'_\chi} \int dq q^2 d\Omega_q \, |F_{\text{DM}}(q, E_\chi)|^2 |f^{nl}_{\text{ion}}(p'_e, q)|^2 S(p'_{\text{e}}) \delta(E_{\text{i}} - E_{\text{f}}) \quad (5.7)$$

where $d\Omega_q = 2\pi d(\cos\theta_q)$ and S is as previously defined the Sommerfeld enhancement factor of the outgoing electron. The energy-conserving delta function with an argument $E_{\text{i}} - E_{\text{f}} = E_d$ can be expressed as a function of $\cos\theta_q$

$$\begin{aligned} f(\cos\theta_q) = E_d = E_\chi - E'_\chi &= E_\chi - \sqrt{(\vec{p}_\chi - \vec{q})^2 + m_\chi^2} \\ &= E_\chi - \sqrt{\vec{p}_\chi^{\,2} + \vec{q}^{\,2} - 2p_\chi q \cos\theta_q + m_\chi^2} \end{aligned} \quad (5.8)$$

and worked out to resolve the angular integral yields

$$\delta(f(\cos\theta_q)) = \frac{E'_\chi}{p_\chi q} \delta(\cos\theta_q - \cos\theta_{q0}). \quad (5.9)$$

Since there is no further dependence on θ_q, the angular integration is trivial. The differential cross-section will thus yield

$$\frac{d\sigma^i v}{d\ln E_R} = \frac{\bar{\sigma}_e}{8\,\mu_{\chi e}^2} \frac{m_\chi^2}{E_\chi p_\chi} \int_0^\infty dq\, q |F_{\text{DM}}(q, E_\chi)|^2 |f^{nl}_{\text{ion}}(p'_e, q)|^2 S(p'_{\text{e}}) \quad (5.10)$$

To obtain the thermally averaged cross-section for a relativistic χ particle, an integration over the energy spectrum dN/dE_χ of the DM decay needs to be taken

$$\begin{aligned} \frac{d\langle\sigma^i v\rangle}{d\ln E_R} &= \int dE_\chi \frac{d\sigma^i v}{d\ln E_R} \frac{dN}{dE_\chi} \\ &= \frac{\bar{\sigma}_e}{8\,\mu_{\chi e}^2} \int_0^\infty dq\, q |f^{nl}_{\text{ion}}(p'_e, q)|^2 S(p'_{\text{e}}) \int_{E_\chi^{\text{min}}}^\infty dE_\chi |F_{\text{DM}}(q, E_\chi)|^2 \frac{m_\chi^2}{E_\chi p_\chi} \frac{dN}{dE_\chi} \end{aligned} \quad (5.11)$$

There is a minimum energy that is needed in order to kick out an electron from the Xe atom as discussed in Sec. 4.2. It is attained when the vectors $\vec{p}_\chi$ and $\vec{q}$ are parallel, or when $\cos\theta_q = 1$ in (5.8), from which two solutions for the associated minimum DM momentum follow, one of which yields a positive deposited energy.

The minimum momentum reads

$$p_\chi^{\min}(q) = \frac{q}{2} + \frac{E_d}{2}\frac{\sqrt{(q^2 - E_d^2)(q^2 - E_d^2 + 4m_\chi^2)}}{q^2 - E_d^2}. \tag{5.12}$$

In the non-relativistic limit $p_\chi^{\min}(q) \approx m_\chi v_{\min}(q)$ and using $q \ll m_\chi$ and $E_d \ll q$ we can recover the solution of the minimum DM velocity as in (4.4).

The differential event rate is obtained by summing over all orbital states in the differential scattering cross-section, times the number of target nuclei per unit mass N_T, times the differential galactic and extragalactic particle fluxes

$$\begin{aligned}\frac{dR_{\text{ion}}}{d\ln E_R} &= N_T \sum_i \int dE_\chi \frac{d\sigma^i}{d\ln E_R}\left(\frac{dJ_{\text{g}}}{dE_\chi} + \frac{dJ_{\text{eg}}}{dE_\chi}\right) \\ &\equiv N_T \frac{\bar{\sigma}_e}{8\,\mu_{\chi e}^2} \sum_i \int_0^\infty dq\, q |f_{\text{ion}}^{nl}(p_e', q)|^2 S(p_{\text{e}}')[I_{\text{g}}(q) + I_{\text{eg}}(q)]\end{aligned} \tag{5.13}$$

where the galactic, J_{g}, and extragalactic, J_{eg}, particle fluxes are obtained in Chapter 3 and $I_{\text{g}}(q)$ and $I_{\text{eg}}(q)$ are the energy integrals corresponding to these fluxes respectively, summarised below

$$I_i(q) = \int_{E_\chi^{\min}(q)}^\infty dE_\chi |F_{\text{DM}}(q, E_\chi)|^2 \frac{m_\chi^2}{E_\chi p_\chi}\frac{dJ_i}{dE_\chi}, \qquad i = \text{g, eg} \tag{5.14}$$

For the galactic particle flux, we apply a monochromatic energy spectrum (3.4) with an injection energy $E_{\text{in}} = m_\psi/2$. This yields the following energy integral

$$\begin{aligned} I_{\text{g}}(q) &= \bar{J}_{\text{g}} \frac{m_\chi^2}{E_{\text{in}}\sqrt{E_{\text{in}}^2 - m_\chi^2}} |F_{\text{DM}}(q, E_{\text{in}})|^2 \Theta\left(E_{\text{in}} - E_\chi^{\min}(q)\right) \\ \bar{J}_{\text{g}} &= 1.1 \times 10^4\, (\text{cm}^2\,\text{s}\,\text{sr})^{-1} \zeta \left(\frac{100\,\text{Gyr}}{\tau_\psi}\right)\left(\frac{100\,\text{MeV}}{m_\psi}\right) e^{-\frac{13.8\,\text{Gyr}}{\tau_\psi}}\end{aligned} \tag{5.15}$$

The extragalactic contribution has a distribution given by (3.26), which can be summarised as follow

$$\begin{aligned}\frac{dJ_{\text{eg}}}{dE_\chi} &= \bar{J}_{\text{eg}} \Pi(E_\chi)\Theta(E_{\text{in}} - E_\chi) \\ \bar{J}_{\text{eg}} &= 1.6 \times 10^4\, (\text{cm}^2\,\text{s}\,\text{sr})^{-1} \zeta \left(\frac{100\,\text{Gyr}}{\tau_\psi}\right)\left(\frac{100\,\text{MeV}}{m_\psi}\right),\end{aligned} \tag{5.16}$$

where $\Pi(E_\chi)$ is, compared to the galactic flux, an extra factor which, as we can prove

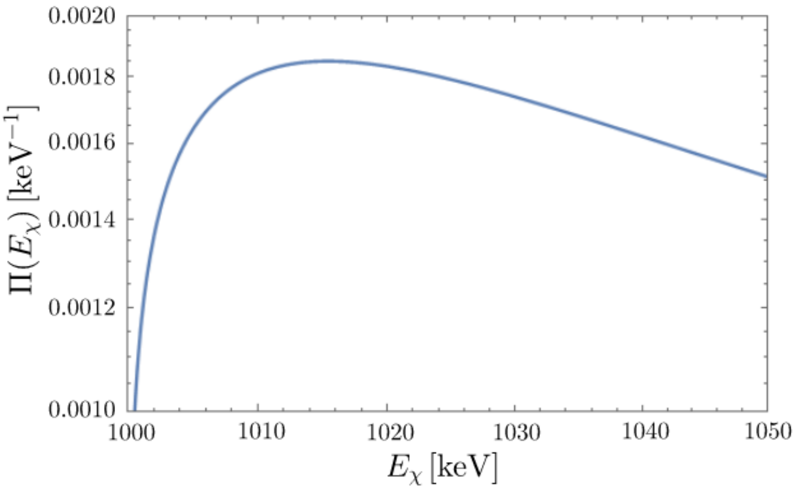

Figure 5.1: An example of how the extra factor $\Pi(E_\chi)$ behaves as a function of energy, due to the expansion of the Universe, in the extragalactic energy fluxes. A dark particle with mass $m_\chi = 1$ MeV and a DM particle with mass $m_\psi = 2.1$ MeV with a decay time of $\tau_\psi = 100$ Gyr, is used in this example.

later, acts to suppress the extragalactic flux. This is given by

$$\Pi(E_\chi) = \frac{\beta(E_\chi)^{1/2}(\kappa\beta(E_\chi)^3+1)^{-1/2}}{E_{\text{in}}v_{\text{in}}\left(\sqrt{\kappa\beta(E_\chi)^3+1}+\sqrt{\kappa\beta(E_\chi)^3}\right)^{\frac{11.6\,\text{Gyr}}{\tau_\psi}}}, \text{ where}$$
$$\beta(E_\chi) = \frac{E_\chi v_\chi}{E_{\text{in}}v_{\text{in}}} \leq 1 \text{ and } \kappa \simeq 2.24. \tag{5.17}$$

The corresponding energy integral $I_{\text{eg}}(q)$, which can be solved numerically[7] gives

$$I_{\text{eg}}(q) = \bar{J}_{\text{eg}}\int_{E_\chi^{\text{min}}(q)}^{E_{\text{in}}} dE_\chi \frac{m_\chi^2}{E_\chi\sqrt{E_\chi^2-m_\chi^2}}|F_{\text{DM}}(q,E_\chi)|^2\Pi(E_\chi). \tag{5.18}$$

Fig. (5.1) shows the behaviour of the factor $\Pi(E_\chi)$ as a function of E_χ for a dark particle with mass $m_\chi = 1$ MeV, that has originated from a DM particle with mass $m_\psi = 2.1$ MeV with a decay time of $\tau_\psi = 100$ Gyr. It is evident that the extragalactic fluxes will have a smaller contribution to the event rate, compare to the event rate from galactic fluxes.

---

[7] All numerical calculations have been performed with Mathematica [58].

5.4 Results

In this framework the differential event rate (5.13), besides the recoil energy E_R, depends on seven other parameters: (i) the DM mass m_ψ, (ii) the dark particle's mass m_χ, (iii) the DM decay time τ_ψ, (iv) the dark photon mass m_V, (v) the fraction ζ defined in (3.2), (vi) the coupling of the dark particle to the dark photon g_D (g_S) and (vii) the kinetic mixing ϵ defined in (2.1). The last two enter into the total elastic cross-section $\bar{\sigma}_e$ (4.12) through the squared matrix element (2.10) as in (4.42). Finally the dark particle can either be a fermion or a scalar, which alters the form of F_{DM} as in (5.4) and (5.5) respectively[8].

Some of these parameters have a rather trivial dependence in the event rate, such as the fraction ζ, which has a linear dependence as can be seen from (5.15)–(5.16). Likewise the DM decay time τ_ψ has a nearly linear dependence, with the exponential factors in both (5.15) and (5.17) not playing a significant role as long as $\tau_\psi \gg t_0 = 13.8$ Gyr. For this reason we fix those two parameters throughout the entire calculation with the values $\tau_\psi = 100$ Gyr, meaning that, statistically, most of the DM particles ψ will decay in the future and $\zeta = 0.1$, meaning that ψ made up one tenth of the entire DM density at the time the CMB was released.

A very important parameter, that ultimately determines the strength of the event rate, is the total elastic cross-section $\bar{\sigma}_e$. Currently within our theoretical framework, no constraints on the $\bar{\sigma}_e - m_\chi$ parameter space have yet been derived from experimental results that are specific to the studied model. We explore the sensitivity of past and current LXe direct detection experiments, XENON10 and XENON1T [59], respectively, to the expected electron recoil rate. After an electron recoils with energy E_R, an approximate additional number of E_R/W electrons are being ionized [60], where $W = 13.8$ eV [61] is the average excitation energy. Whereas XENON10 has the best sensitivity to events with only few electrons, XENON1T has the current best sensitivity at larger electron multiplicity, i.e. at energy deposits.

The 90% C.L. upper limit on the single-electron event rate in XENON10 is 23.4 /kg/day [62], constraining the event rate with $E_R \lesssim 13.8$ eV. The differential electron event rate in XENON1T has not yet been reported. However, an overall electron background rate in the energy range $E_R = 5 - 40$ keV was found to be 1.93×10^{-4} /kg/day/keV ≈ 0.07 /kg/year/keV [63], in good agreement with Monte Carlo predictions [32] shown in Fig. (5.2). We can see that for $E_R = 0 - 250$ keV the electron recoil background rate is expected to be flat, with a total rate of 1.8×10^{-4} /kg/day/keV. We therefore use the number 0.07 /kg/year/keV as a fidu-

---

[8] The parameters used to calculate the event rates, have however shown very little difference between a fermionic and a scalar dark particle in terms of strength and shape of the event rate and thus a scalar dark particle event rate is not explicitely shown in this thesis.

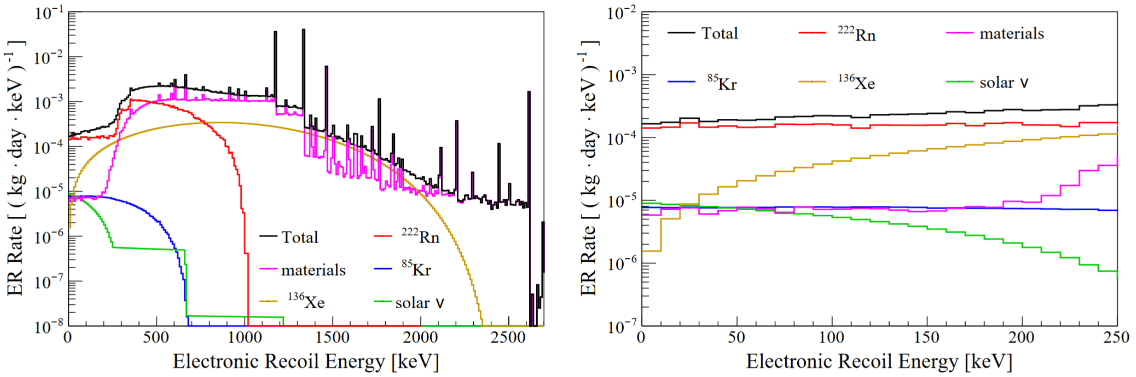

Figure 5.2: Monte Carlo predictions of the electron recoil background in 1 tonne fiducial volume of the XENON1T detector caused by different factors (mainly radioactivity from the detector components) as indicated in the legends. The total contribution from all these factors (black line) amounts to 1.8×10^{-4} (kg·day·keV)$^{-1}$ at low energies, as can be seen in the right side panel, which is the zoom of the left side panel. Figure is taken from [32].

cial upper limit to extract the expected sensitivity from XENON1T, assuming such flat background. A more detailed statistical analysis which requires the modelling of signal formation and electron multiplicity is laborious and beyond the scope of this thesis.

As a first task, we would like to show how the differential event rate behaves with E_R for the different combinations of the parameters of our model. We show how the various shells 1s, 2s,..., 4d contribute to the event rate. Specifically, we look at two cases of mediator regimes: one with a heavy mediator with mass $m_V = 3m_\chi$ and one with a light mediator with mass $m_V = 0.1$ meV. For practical purposes we first consider only the contribution coming from galactic sources and fix $\bar{\sigma}_e$, such that the (expected) upper limit of 0.07 /kg/year/keV at $E_R = 5$ keV for the heavy mediator case and 23.4 /kg/day for energies up to 13.8 eV for the light mediator case are saturated. The reason why we use XENON1T data for the heavy mediator and XENON10 data for the light mediator case, is due to the fact that, as we will demonstrate, in the former case, the event rate peaks towards the kinematic endpoint (a few keV per assumption), while in the latter case it peaks at low E_R.

Examples with heavy mediators are shown in Table 5.1 and examples with light mediators in Table 5.2. In all these examples $\bar{\sigma}_e$ has been extracted (and for simplicity rounded to the closest integer number) so that they yield the a rate that corresponds to the electron recoil background rate. Fig. (5.4) shows event rates for the examples 4 and 9 with a dark particle with mass $m_\chi = 1$ MeV and a DM particle with mass $m_\psi = 2.1$ MeV for both a massive mediator with mass $m_V = 3$ MeV (upper panel) and a light mediator with mass $m_V = 0.1$ meV (lower panel). The solid line is the

	m_χ [MeV]	m_ψ [MeV]	m_V [MeV]	$\bar{\sigma}_e$ [cm^2]
1	100	201	300	10^{-36}
2	10	21	30	2×10^{-37}
3	10	20.1	30	10^{-37}
4	1	2.1	3	10^{-38}
5	0.1	0.25	0.3	2×10^{-40}

Table 5.1: Examples with heavy mediators with mass $m_V = 3m_\chi$ for light dark particles with masses 100 keV up to 100 MeV. The predicted electron recoil background by XENON1T at E_R =5 keV is used to extract $\bar{\sigma}_e$.

	m_χ [MeV]	m_ψ [MeV]	m_V [meV]	$\bar{\sigma}_e$ [cm^2]
6	1000	2001	0.1	8×10^{-34}
7	100	201	0.1	2×10^{-35}
8	10	20.1	0.1	2×10^{-36}
9	1	2.1	0.1	3×10^{-38}
10	0.1	0.25	0.1	10^{-40}
11	0.01	0.03	0.1	2×10^{-43}

Table 5.2: Examples with light mediators with mass $m_V = 0.1$ meV for light dark particles with masses 10 keV up to 1 GeV. XENON10 data at low E_R is used to extract $\bar{\sigma}_e$.

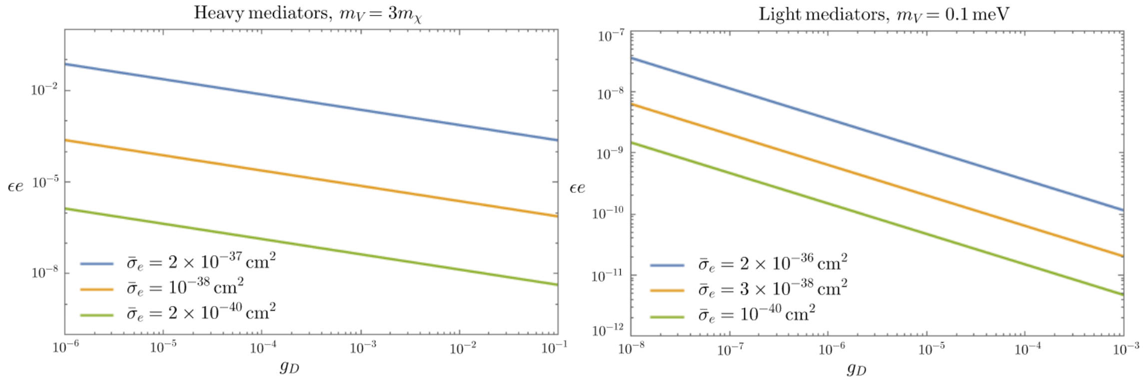

Figure 5.3: Effective coupling, ϵe, as a function of DM coupling, g_D, in three examples with heavy (left) and light mediators (right). Dark particles with the following masses, and their respective extracted $\bar{\sigma}_e$, have been used: 10 MeV (blue), 1 MeV (yellow) and 100 keV (green).

total contribution coming from galactic sources and the dashed lines are the various shell contributions to the event rate as indicated in the legends.

As aforementioned, the visible event rates for heavy mediators lie in the $E_R \sim$keV range, while for light mediators they peak at around 5-10 eV. The shapes of the event rates between these two mediator regimes are also vastly different, due to their difference in the DM form factor, F_{DM}. In the case of heavy mediators, $F_{\text{DM}} \approx 1$, so that the Θ-function in (5.15) sets a sharp cut-off. In the case of light mediators, $F_{\text{DM}} \sim q^{-2}$, so that the rate has a non-linear decline at higher E_R. This is more evident if we observe Fig. (4.1), where higher recoil energies peak at higher transfer momenta. Since F_{DM} for a light mediator is suppressed at high transfer momenta, we expect the contribution of f_{ion} at large E_R to be suppressed too. Therefore the event rate peaks at low recoil energies.

In terms of $\bar{\sigma}_e$, we observe that it increases with increasing m_χ, meaning that the sensitivity decreases at higher masses. This is due to the factor $\mu_{\chi e}^2$ in the denominator of (5.13). The sensitivity also decreases with increasing m_ψ, as can be noticed by the examples 2 and 3 of Table (5.1). This is due to the factor $(1\,\text{GeV}/m_\psi)$ in (5.16), which decreases the rate for larger m_ψ. Furthermore, we note that by choosing $\bar{\sigma}_e$, we effectively choose a combination of parameters such as the kinetic mixing, ϵ, as well as the DM coupling, g_D, such that they fulfil Eq. (4.42). This is shown in Fig. (5.3), where the effective charge, ϵe, is plotted against the DM coupling, g_D, for three examples of dark particles with both heavy (left) and light mediators (right).

In Fig. (5.5) we can see the energy spectrum for selected examples from Tables (5.1) and (5.2) of heavy (left) and light mediators (right). In the heavy mediator case, we show the XENON1T background (dashed grey line), which intersects with

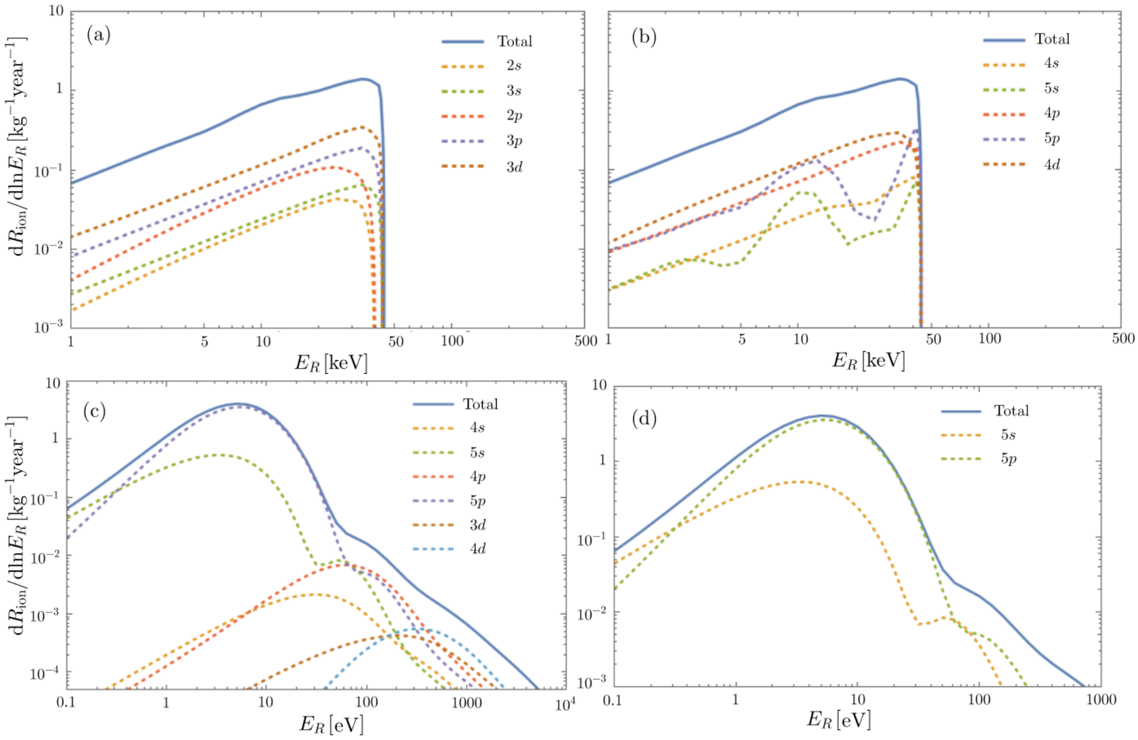

Figure 5.4: Event rates for a dark particle with mass $m_\chi = 1$ MeV and a DM particle with mass $m_\psi = 2.1$ MeV. The blue solid line shows the total contribution coming from galactic sources, while the dashed lines are the individual shell contributions as indicated in the legends. In the **upper panel** a heavy mediator with mass $m_V = 3$ MeV is used, while in the **lower panel** a light mediator with mass $m_V = 0.1$ meV is used. Sub-figures (a) and (b) are complementary to each other, showing the various shell contributions, while sub-figure (d) is the zoom of (c) for a minimum event rate of $10^{-3}\,\rm kg^{-1}year^{-1}$.

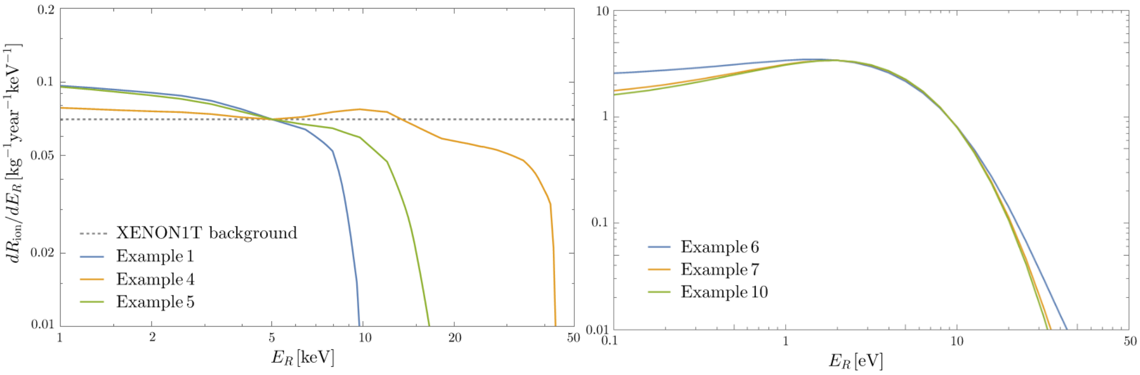

Figure 5.5: Energy spectrum for selected examples of dark particles from Tables (5.1) and (5.2) as indicated in the legends. **Left**: Energy spectrum for heavy mediators that yield an event rate of $0.07\,(\rm kg\,year\,keV)^{-1}$ at $E_R = 5$ keV (dashed line). **Right**: Energy spectrum for light mediators that have a total background rate of $23.4\,(\rm kg\,day)^{-1}$ for electron recoil energies up to 13.8 eV.

the curves at $E_R = 5$ keV. We observe that the energy spectrum is not completely flat, but increases with decreasing E_R. In the light mediator case, the curves appear to be on top of each other, since the event rates are similar for the various cases at low E_R.

In the second possibility we explore the contributions coming from galactic sources against those from extragalactic sources. The event rates for selected examples can be seen in Fig. (5.6), where the blue solid line is the event rate with the total contribution coming from galactic sources and the yellow dashed line shows the contribution from extragalactic sources. We used the extraction of $\bar{\sigma}_e$ as described previously and used it when calculating the event rate from extragalactic fluxes. Specifically, we observe the event rates of examples 4 (upper left) and 3 (lower left) with heavy mediators from Table (5.1) and 9 (upper right) and 8 (lower right) with light mediators from Table (5.2). A general observation is that the contribution from extragalactic fluxes is less than from galactic fluxes. Despite the fact that there are more DM sources outside our galaxy, the factor of expansion suppresses the observation of those sources. This is evident in the extra factor $\Pi(E_\chi)$ defined in (5.17), as discussed in Sec. 5.3.

To understand the magnitude of the impact of the extragalactic to the galactic contribution better, we plot the event rate on a non-logarithmic scale. This can be seen in Fig. (5.7), where the left side shows examples with light mediators and the right side examples with heavy mediators. The differential event rate runs from 0 up to 5 counts per kg per year. We can see that, at least in the case of a dark particle with mass $m_\chi = 1$ MeV (example 9), the extragalactic contribution at $E_R = 5$ eV amounts to 10% that of the galactic contribution. In a large enough tank with 1-2 tonnes of LXe, this can be a significant contribution.

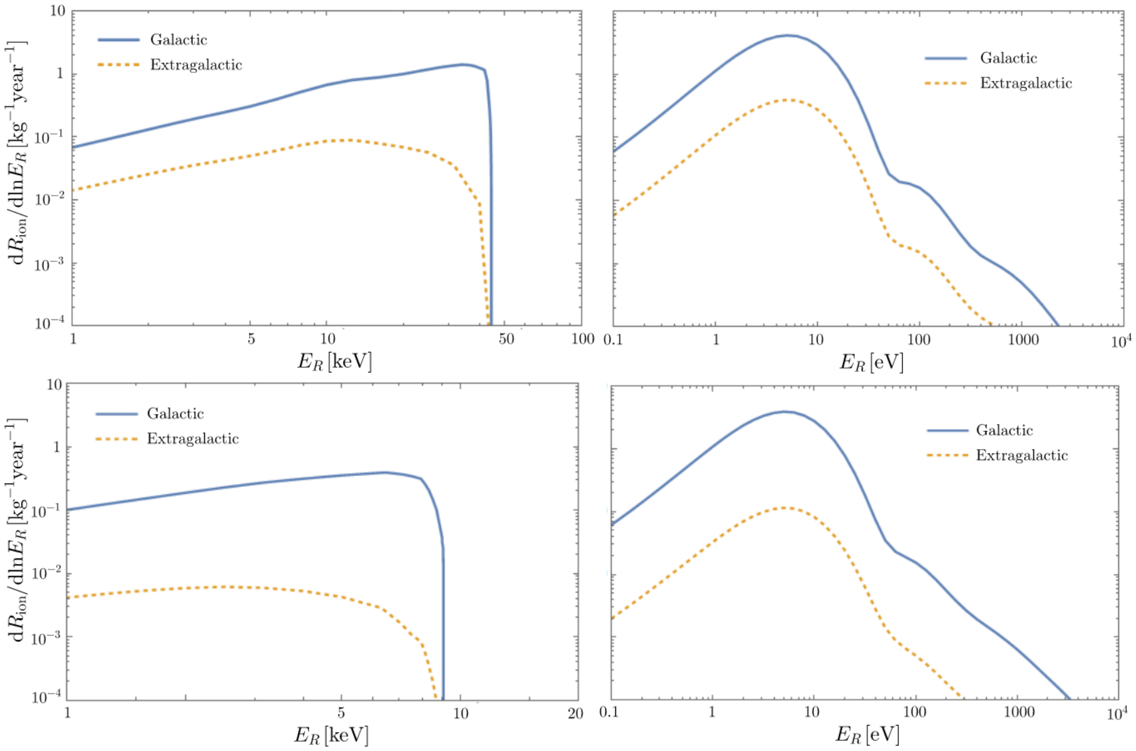

Figure 5.6: Event rates from galactic (solid) and extragalactic (dashed) sources for a dark particle with mass $m_\chi = 1$ MeV and a DM particle with mass $m_\psi = 2.1$ MeV (upper panel) and a dark particle with mass $m_\chi = 10$ MeV and a DM particle with mass $m_\psi = 20.1$ MeV (lower panel). In the left panel we are using heavy mediators with masses $m_V = 3m_\chi$, while a light mediator with mass $m_V = 0.1$ meV is used in the right panel.

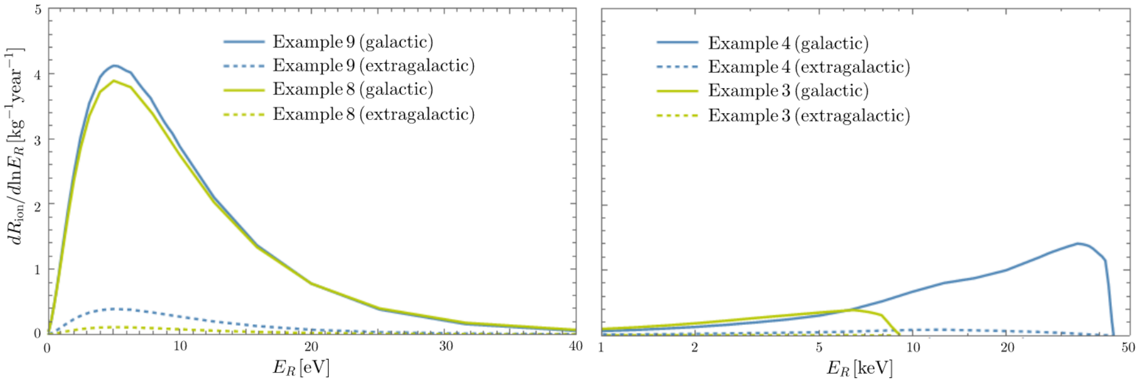

Figure 5.7: Event rates, in a non-logarithmic scale, for selected examples from Tables (5.1) and (5.2) with contributions from galactic (solid lines) and extragalactic sources (dashed lines) for both light (left) and heavy mediators (right).

Chapter 6

Conclusions and Outlook

The goal of this thesis was to study the direct detection event rates coming from the two-body decay of a progenitor DM particle into two dark particles, that ultimately can get detected in a LXe DM search. The dark particle-electron interaction is mediated through a dark photon that kinetically mixes with the photon. The result of this interaction is registered as an electron recoil energy in the detector.

We showed that the shape of the resulting event rate is affected by the various parameters of our model, like the dark particle's mass m_χ, the DM mass m_ψ and whether the dark photon is heavy or light, which alters the form of the DM form factor, F_{DM}. Specifically we looked at two mediator regimes, one where the mediator has a mass $m_V = 3m_\chi$ and one where the mediator is light, with mass $m_V = 0.1$ meV. We showed that the former has event rates in the keV electron recoil energy range, contrary to the latter, which has the event rate peak at the eV energy range. Other parameters of our model, such as the DM decay time τ_ψ and the fraction ζ affect the event rate through a simple overall scaling factor.

The event rate further involves the total elastic cross-section, $\bar{\sigma}_e$, which encodes the dependence on the dark coupling, g_D, and the kinetic mixing, ϵ. In our numerical analysis, we considered the predicted electron recoil background of the XENON1T detector [63], to extract the sensitivity on $\bar{\sigma}_e$, for a combination of parameters in the heavy mediator regime. Since the light mediator regime is mostly sensitive to very low electron recoil energies, we have considered the XENON10 data [62] and extracted the sensitivity on $\bar{\sigma}_e$ for those parameters.

Finally, we have calculated a flux coming from extragalactic sources and obtained the corresponding event rates coming from those sources, with the combination of parameters used to obtain event rates from galactic sources. We showed that for chosen combination of parameters, it can yield as much as a 10% of that of an event rate from galactic sources; the relative importance of the galactic vs. the extragalactic flux depends most sensitively on the progenitor lifetime, τ_ψ.

Our analysis considered 2-body decays, i.e. a monochromatic energy spectrum. However, a progenitor could decay into more particles with continuously distributed energies. This would change the resulting galactic and extragalactic particle fluxes and by that, the resulting event rates and the sensitivity on $\bar{\sigma}_e$. Furthermore our considered toy model has parameters, such as the fraction ζ and the DM decay time τ_ψ, which would need to be put into the bigger experimental and cosmological model.

A light sector of new particles, such as the one that is proposed here, is most notably constrained through astrophysics, high-intensity, low-energy collider experiments, and through cosmology. For example, a cosmological density of dark states will be created through the same coupling with electrons that is responsible for the direct detection. The efficiency of this process depends not only on the kinetic mixing parameter ϵ, but also if the dark photon can be created on-shell in electron-positron annihilation in the early universe, i.e. if $m_V > 2m_e$. Achieving a successful cosmological history with simultaneously respecting all available constraints is a non-trivial task, and requires a dedicated study that goes beyond the scope of this work. Finally, we have not specified the origin of the longevity of the progenitor against decay as well as any further details that would make it qualify as a successful dark matter candidate.

The crucial outcome of this analysis is the detailed calculation of event rates for a representative model of dark states that are sourced by decaying dark matter with a lifetime possibly much larger than the age of the universe. It is entirely possible that our universe is filled with such dark radiation, and an understanding of its potential experimental signatures is therefore an important task. We have focused on the interaction of dark states with electrons, allowing to detect very low-energetic particles and thereby energy deposits, from the eV scale to several keV, with liquid xenon type dark matter detectors. Such “non-standard” searches performed on existing and future data of direct detection experiments hence diversify their physics output.

Appendices

Appendix A

Kinematics

A.1 Kinematic invariances

Reference frames are defined by the properties of the initial state of a collision process. For relativistic processes, a transformation from one system of reference to another, that moves with a constant relative velocity, is carried out via Lorentz transformations. Relevant to our calculation is the transformation of the energies and momenta of particles from the target system (TS), denoted with ^{T}, to the center-of-mass system (CMS), denoted with *, and vice versa. This is carried out with a Lorentz boost, L, as follows

$$p^* = \begin{pmatrix} E^* \\ \vec{\mathrm{p}}^* \end{pmatrix} = L\, p^T = \begin{pmatrix} \gamma & -\gamma\vec{\mathrm{v}}_{\mathrm{CM}} \\ -\gamma\vec{\mathrm{v}}_{\mathrm{CM}} & 1 + \dfrac{\gamma^2}{1+\gamma}\vec{\mathrm{v}}^2_{\mathrm{CM}} \end{pmatrix} \begin{pmatrix} E^T \\ \vec{\mathrm{p}}^T \end{pmatrix}, \tag{A.1}$$

where $\vec{\mathrm{v}}_{\mathrm{CM}}$ is the velocity of the CMS in the TS and γ the corresponding Lorentz factor (see below). Therefore the individual energy and momentum of a colliding particle in the CMS will yield

$$\begin{aligned} E^* &= \gamma(E^T - \vec{\mathrm{v}}_{\mathrm{CM}} \cdot \vec{\mathrm{p}}^T) \\ \vec{\mathrm{p}}^* &= \vec{\mathrm{p}}^T + \gamma\vec{\mathrm{v}}_{\mathrm{CM}} \left(\frac{\gamma\vec{\mathrm{v}}_{\mathrm{CM}} \cdot \vec{\mathrm{p}}^T}{1+\gamma} - E^T \right), \end{aligned} \tag{A.2}$$

where the velocity of the CMS for two colliding particles with four momenta $p_1 = p_1^\mu$ and $p_2 = p_2^\mu$ is by definition given by

$$\mathrm{v}_{\mathrm{CM}} = \left. \frac{|\vec{p}_1 + \vec{p}_2|}{E_1 + E_2} \right|_{p_2^T = 0} = \frac{p_1^T}{E_1^T + m_2}, \tag{A.3}$$

where m_2 is the rest mass of the target particle. The corresponding Lorentz factor yields

$$\gamma = \frac{1}{\sqrt{1-\mathrm{v}_{\mathrm{CM}}^2}} = \frac{E_1^T + m_2}{\sqrt{s}}, \tag{A.4}$$

where s is the invariant mass of the system defined as the sum of the incoming 4-momenta $s = (p_1 + p_2)^2$. s has the same value in all reference frames and is hence called an invariant. The invariant treatment of 2 → 2 scattering will prove to be important for theoretical purposes. Therefore we will express all quantities in terms of Lorentz invariants.

Next to the invariant mass s, there are 2 further invariant variables, the invariant momentum transfer t and the crossing variable u. They are called the Mandelstam variables and can be summarized below

$$\begin{aligned}
s &= (p_1 + p_2)^2 = (p_3 + p_4)^2 \\
&= (E_1^* + E_2^*)^2 = (E_3^* + E_4^*)^2 \\
&= m_1^2 + m_2^2 + 2m_2E_1^T && \text{(A.5)} \\
t &= (p_1 - p_3)^2 = (p_2 - p_4)^2 \\
&= 2m_1^2 - 2E_1E_3 + 2p_1p_3\cos\theta_1 \\
&= 2m_2^2 - 2m_2E_4^T && \text{(A.6)} \\
u &= (p_1 - p_4)^2 = (p_2 - p_3)^2 \\
&= m_1^2 + m_2^2 - 2E_1E_4 + 2p_1p_4\cos\theta_2 \\
&= m_1^2 + m_2^2 - 2m_2E_3^T, && \text{(A.7)}
\end{aligned}$$

where we are considering the elastic scattering between two particles in the process $p_1 + p_2 \to p_3 + p_4$. The Mandelstam variables are also related with each other in the following equation

$$s + t + u = 2(m_1^2 + m_2^2). \tag{A.8}$$

We can express energies and momenta in both reference frames in terms of these relativistic invariants. For example the incoming energy of particle 1 in the TS is derived from (A.5)

$$E_1^T = \frac{s - m_1^2 - m_2^2}{2m_2}, \tag{A.9}$$

with a corresponding target frame three-momentum

$$\begin{aligned}(p_1^T)^2 &= (E_1^T)^2 - m_1^2 \\ &= \frac{(s - m_1^2 - m_2^2)^2 - 4m_1^2 m_2^2}{4m_2^2} \\ &\equiv \frac{\lambda(s, m_1^2, m_2^2)}{4m_2^2}, \end{aligned} \tag{A.10}$$

where $\lambda(x, y, z)$ is the triangle function defined as $\lambda(x, y, z) = (x - y - z)^2 - 4yz$. Similarly the three-momentum in the CMS can be expressed in terms of the invariant s, as follows

$$(p_1^*)^2 = \frac{\lambda(s, m_1^2, m_2^2)}{4s}. \tag{A.11}$$

An important measurement quantity is the recoil energy, E_R, of the target particle. This is defined as the kinetic energy in the TS of the target particle and is given by $E_R = E_4^T - m_2$, where E_4 is the final energy of the recoiled particle. In terms of the invariant momentum, following (A.6), it is given by

$$t = -2m_2 E_R. \tag{A.12}$$

With the help of these invariant quantities, we can construct in the next section an invariant differential cross-section.

A.2 Differential cross section

The total reaction cross section of a 2 → n process is generally given by the following expression (following the notation by [64])

$$\sigma_n(s, m_i) = \frac{1}{F} I_n(s), \tag{A.13}$$

where $F = 2\sqrt{\lambda(s, m_1^2, m_2^2)}$ is the flux factor and I_n is the phase space integral given by

$$I_n(s) = \int \prod_{i=3}^{n+2} \frac{d^3 p_i}{(2\pi)^{3n}\, 2E_i} (2\pi)^4 \delta^{(4)}(p_1 + p_2 - \sum_i p_i) \left|\mathcal{M}(\vec{p}_i)\right|^2, \tag{A.14}$$

where the factor $|\mathcal{M}(\vec{p}_i)|^2$ is the squared matrix element, which for free propagating particles is given by the matrix element using plane waves

$$\begin{aligned} < \vec{p}_3, ..., \vec{p}_n \, |\mathcal{M}| \, \vec{p}_1, \vec{p}_2 > &= \int d^3 r e^{-i(\sum_i \vec{p}_i - \vec{p}_1 - \vec{p}_2)\cdot\vec{r}} \mathcal{M}(\vec{p}_i) \\ &= (2\pi)^3 \delta^{(3)}(\vec{p}_1 + \vec{p}_2 - \sum_i \vec{p}_i) \mathcal{M}(\vec{p}_i). \end{aligned} \qquad \text{(A.15)}$$

We would like to evaluate the integral (A.14) in the CMS and TS for the simple case of 2 → 2 scattering. If we are interested only on a differential cross section, then no integration over $|\mathcal{M}|^2$ is needed, thus we can treat this as a constant. For the CMS, one may start by integrating over the 4-momentum p_4 by using the 4-dimensional δ-function and resolving the 3-dimensional momentum space element $d^3 p_3$ in spherical coordinates. This yields

$$I_2^*(s) = \frac{p_3^*}{16\pi^2 \sqrt{s}} \int d\Omega^* \, |\mathcal{M}|^2 \, . \qquad \text{(A.16)}$$

If no further integration over the solid angle is taken, then the differential cross section, given the flux factor is $F = 4\sqrt{s} p_1^*$, will be for $p_1 * = p_3 *$

$$\frac{d\sigma}{d\Omega^*} = \frac{\overline{|\mathcal{M}|^2}}{64\pi^2 s}. \qquad \text{(A.17)}$$

For the TS, one may take a similar approach by expressing the 4-dimensional δ-function as a 3-dimensional momentum and 1-dimensional energy δ-functions and then take the integration over p_4. Evaluating all the δ-functions and taking the integral over p_3, one arrives to the following expression for the differential cross section

$$\frac{d\sigma}{d\Omega^T} = \frac{1}{64\pi^2 m_2 p_1^T} \frac{(p_3^T)^2}{p_3^T (E_1^T + E_2^T) - E_3^T p_1^T \cos\theta^T} \, |\mathcal{M}|^2 \, . \qquad \text{(A.18)}$$

To express the cross sections (A.17) and (A.18) in terms of the invariant cross section $d\sigma/dt$ we utilize (A.6) by differentiating both sides and arrive to the following expression

$$\frac{d\sigma}{dt} = \frac{d\sigma}{d\Omega^*} \frac{d\Omega^*}{dt} = \frac{|\mathcal{M}|^2}{64\pi \, s \, p_1^{*2}} = \frac{|\mathcal{M}|^2}{16\pi \, \lambda(s, m_1^2, m_2^2)}. \qquad \text{(A.19)}$$

Finally, the differential cross section over the recoil energy follows from (A.12) with $d\,|t| = 2m_2 dE_R^T$, yielding

$$\frac{d\sigma}{dE_R^T} = \frac{d\sigma}{dt} \frac{dt}{dE_R^T} = \frac{m_2 \, |\mathcal{M}|^2}{8\pi \, \lambda(s, m_1^2, m_2^2)}. \qquad \text{(A.20)}$$

Acknowledgements

I would like to thank my adviser Josef Pradler, for the envision of this work on the exciting topic of dark matter research. I am grateful for his outstanding support, supervision and guidance throughout the course of this project. I would also like to thank my university supervisor André H. Hoang, for his encouragement and contribution he gave me to the better understanding of particle physics.

Equally, I would like to thank the High Energy Physics Institute (HEPHY) of the Austrian Academy of Science (ÖAW) for their financial contribution and enablement of this project, as well as for providing me a workspace. In addition, I would like to thank the Dark Matter theory group, including Suchita Kulkarni, Xiaoyong Chu and Lukas Semmelrock for many great discussions on interesting topics and the enjoyable time at HEPHY.

Finally, I am grateful to my fiancé for his encouragement and emotional support he has unequivocally given me throughout the course of this journey.

Bibliography

[1] K. Nakamura et al. (Particle Data Group), Journal of Physics **G37** (2010) 075021.

[2] K. G. Begeman, A. H. Broeils, R. H. Sanders, *Extended rotation curves of spiral galaxies: Dark haloes and modified dynamics*, Mon. Not. R. astr. Soc. **249** (1991) 523-537.

[3] D. Clowe et al., *A direct empirical proof of the existence of dark matter*, Astrophys. J. **648** (2006) L109-L113, [astro-ph/0608407].

[4] D. J. Fixsen, *The Temperature of the Cosmic Microwave Background*, Astrophys. J. **707** (2): 916–920 (2006), [arXiv:0911.1955].

[5] P. A. R. Ade et al. (Planck Collaboration), *Planck 2013 results. XVI. Cosmological parameters*, [arXiv:1303.5076].

[6] Paczynski, B., *Gravitational microlensing by the galactic halo*, Astrophys. J. **304** (1986) 1.

[7] Griest, K., *Galactic microlensing as a method of detecting massive compact halo objects*, Astrophys. J. **366** (1991) 412.

[8] N. Palanque-Delabrouille et al., *Neutrino masses and cosmology with Lyman-alpha forest power spectrum*, JCAP **11** (2015) 011.

[9] Cosmology Part III Mathematical Tripos, lecture notes by Daniel Baumann, http://www.damtp.cam.ac.uk/user/db275/Cosmology/Lectures.pdf.

[10] H. Murayama, *Physics Beyond the Standard Model and Dark Matter*, [arXiv:0704.2276].

[11] H. Mo, F. V. D. Bosch, S. White, *Galaxy formation and evolution*, 2010 Edition.

[12] G. Bertone, D. Hooper, J. Silk, *Particle Dark Matter: Evidence, Candidates and Constraints*, Phys. Rept. **405**, (2005) 279-390, [hep-ph/0404175].

[13] J. F. Navarro, C. S. Frenk, S. D. M. White, *The Structure of Cold Dark Matter Halos*, Astrophys. J. **462**, (1996) 563-575, [astro-ph/9508025].

[14] J. F. Navarro, C. S. Frenk, S. D. M. White, *A Universal Density Profile from Hierarchical Clustering*, Astrophys. J. **490** (1997) 493-508, [astro-ph/9611107].

[15] B. Moore, T. Quinn, F. Governato, J. Stadel, G. Lake, *Cold collapse and the core catastrophe*, Mon. Not. Roy. Astron. Soc. **310** (1999) 1147-1152, [astro-ph/9903164].

[16] M. Weber, W. d. Boer , *Determination of the Local Dark Matter Density in our Galaxy*, Astron. Astrophys. **509**:A25 (2010) [arXiv:0910.4272].

[17] R. Catena, P. Ullio, *A novel determination of the local dark matter density*, JCAP **1008** (2010) 004, [arXiv:0907.0018].

[18] IAU Commission 33 (1985).

[19] A. M. Green, *Astrophysical uncertainties on direct detection experiments*, Mod. Phys. Lett. A **27** (2012) 1230004, [arXiv:1112.0524].

[20] M.C. Smith et al., *The RAVE Survey: Constraining the Local Galactic Escape Speed*, Mon. Not. Roy. Astron. Soc. **379** (2007) 755-772, [astro-ph/0611671].

[21] R. Schoenrich, J. Binney, W. Dehnen, *Local Kinematics and the Local Standard of Rest*, Mon. Not. Roy. Astron. Soc. **403** (4) (2010) 1829-1833, [arXiv:0912.3693].

[22] K. Freese, M. Lisanti, *Annual Modulation of Dark Matter: A Review*, Rev. Mod. Phys., **85** (2013) 1561, [arXiv:1209.3339].

[23] J. D. Lewin, P. F. Smith, *Review of mathematics, numerical factors, and corrections for dark matter experiments based on elastic nuclear recoil*, Astropart. Phys. **6** (1996) 87-112.

[24] The XENON Dark Matter Project, http://xenon.astro.columbia.edu/

[25] LUX Dark Matter, http://luxdarkmatter.org/

[26] ZEPLIN-III, http://www.hep.ph.ic.ac.uk/ZEPLIN-III-Project/

[27] T. Saab, *An Introduction to Dark Matter Direct Detection Searches & Techniques*, [arXiv:1203.2566].

[28] J. Angle et al. (XENON10 Collaboration), *First Results from the XENON10 Dark Matter Experiment at the Gran Sasso National Laboratory*, Phys. Rev. Lett. **100** (2008) 021303, [arXiv:0706.0039].

[29] E. Aprile et al. (XENON100 Collaboration), *First Dark Matter Results from the XENON100 Experiment*, Phys. Rev. Lett. **105** (2010) 131302, [arXiv:1005.0380].

[30] E. Aprile et al. (XENON100 Collaboration), *Dark Matter Results from 225 Live Days of XENON100 Data*, Phys. Rev. Lett. 109 (2010) 181301, [arXiv:1207.5988v2].

[31] E. Aprile et al. (XENON100 Collaboration), *XENON100 Dark Matter Results from a Combination of 477 Live Days*, Phys. Rev. Lett. D94 (2016) 122001, [arXiv:1609.06154v3].

[32] E. Aprile et al. (XENON Collaboration), *Physics reach of the XENON1T dark matter experiment*, JCAP04 (2016) 027, [arXiv:1512.07501].

[33] T. M. Undagoitia, L. Rauch, *Dark matter direct-detection experiments*, J. Phys. 013001 **G43** (2016) 1, [arXiv:1509.08767].

[34] IceCube collaboration: R. Abbasi *et al.*, *Limits on a muon flux from neutralino annihilations in the Sun with the IceCube 22-string detector*, Phys. Rev. Lett. **102** (2009) 201302, [arXiv:0902.2460].

[35] Fermi-LAT collaboration: A. A. Abdo *et al.*, *Constraints on Cosmological Dark Matter Annihilation from the Fermi-LAT Isotropic Diffuse Gamma-Ray Measurement*, JCAP **1004** (2010) 014, [arXiv:1002.4415].

[36] PAMELA Collaboration, O. Adriani et al., *Observation of an anomalous positron abundance in the cosmic radiation*, Nature **458** (2009) 607–609, [arXiv:0810.4995].

[37] M. Beltran, D. Hooper, E. W. Kolb, Z. A. C. Krusberg, T. M. P. Tait *Maverick dark matter at colliders*, JHEP **1009** (2010) 037, [arXiv:1002.4137].

[38] N. Arkani-Hamed, D. P. Finkbeiner, T. R. Slatyer, N. Weiner, *A Theory of Dark Matter*, Phys. Rev. **D79** (2009) 015014, [arXiv:0810.0713].

[39] M. Pospelov, A. Ritz, *Astrophysical Signatures of Secluded Dark Matter*, Phys. Lett. **B671** (2009) 391-397, [arXiv:0810.1502v2].

[40] A. Sommerfeld, *Über die Beugung und Bremsung der Elektronen*, Annalen der Physik **403** 3 (1931) 257-330.

[41] PAMELA Collaboration: O. Adriani *et al.*, *PAMELA results on the cosmic-ray antiproton flux from 60 MeV to 180 GeV in kinetic energy*, Phys. Rev. Lett. **105** (2010) 121101, [arXiv:1007.0821].

[42] The Fermi LAT Collaboration, A. A. Abdo et al., *Measurement of the Cosmic Ray* $e^+ + e^-$ *spectrum from 20 GeV to 1 TeV with the Fermi Large Area Telescope*, Phys. Rev. Lett. **102** (2009) 181101, [arXiv:0905.0025].

[43] The Fermi LAT Collaboration, M. Ackermann et al., *Measurement of separate cosmic-ray electron and positron spectra with the Fermi Large Area Telescope*, Phys. Rev. Lett. **108** (2012) 011103, [arXiv:1109.0521].

[44] AMS Collaboration, M. Aguilar et al., *First Result from the Alpha Magnetic Spectrometer on the International Space Station: Precision Measurement of the Positron Fraction in Primary Cosmic Rays of 0.5 – 350 GeV*, Phys. Rev. Lett. **110** (2013) Nr. 14 141102.

[45] M. Lisanti, *Lectures on Dark Matter Physics*, [arXiv:1603.03797].

[46] J. Alexander, M. Battaglieri, B. Echenard, R. Essig et al., *Dark Sectors 2016 Workshop: Community Report*, [arXiv:1608.08632]

[47] L.B. Okun, *Limits of electrodynamics: paraphotons?*, JETP **56**, 502 (1982).

[48] B. Holdom, *Two U(1)'s and epsilon charge shifts*, Phys. Lett. B **166**, 196 (1986).

[49] H. An, M. Pospelov and J. Pradler, *New stellar constraints on dark photons*, Phys. Rev. Lett. **B725** (2013) 190, [arXiv:1302.3884].

[50] M. Cirelli et al., *PPPC 4 DM ID: A Poor Particle Physicist Cookbook for Dark Matter Indirect Detection*, JCAP **1103** (2011) 051, [arXiv:1012.4515].

[51] R. Essig, J. Mardon, T. Volansky, *Direct Detection of Sub-GeV Dark Matter*, Phys. Rev. Lett. **D85** (2012) 076007, [arXiv:1108.5383].

[52] R. Essig, A. Manalaysay, J. Mardon, P. Sorensen, T. Volansky, *First Direct Detection Limits on sub-GeV Dark Matter from XENON10*, Phys. Rev. Lett. **109**, (2012) 021301, [arXiv:1206.2644].

[53] M. Abramowitz, I. A. Stegun, *Handbook of mathematical functions.*

[54] C. C. J. Roothaan, *Self-Consistent Field Theory for Open Shells of Electronic Systems*, Rev. Mod. Phys. **32** (2) (1960) 179-185.

[55] E. Clementi, C. Roetti, *Atomic Data and Nuclear Data Tables*, **14**:3-4 (1974) 177-478.

[56] C. F. Bunge, J. A. Barrientos, A. V. Bunge, *Atomic Data and Nuclear Data Tables*, **53** (1) (1993) 113-162.

[57] S. K. Lee, M. Lisanti, S. Mishra-Sharma, B. R. Safdi, *Modulation Effects in Dark Matter-Electron Scattering Experiments*, Phys. Rev. Lett. **D92** (2015) 083517, [arXiv:1508.07361].

[58] Wolfram Research, Inc., Mathematica, Version 11.0, Champaign, IL (2017).

[59] The XENON1T Experiment, http://www.xenon1t.org/

[60] R. Essig, T. Volansky, T.T. Yu, *New Constraints and Prospects for sub-GeV Dark Matter Scattering off Electrons in Xenon*, Phys. Rev. **D96**, (2017) 043017, [arXiv:1703.00910]

[61] T. Doke, A. Hitachi, J. Kikuchi, K. Masuda, H. Okada, and E. Shibamura, *Absolute Scintillation Yields in Liquid Argon and Xenon for Various Particles*, Japanese Journal of Applied Physics **41**, 1538 (2002).

[62] R. Essig, A. Manalaysay, J. Mardon, P. Sorensen, T. Volansky, *First Direct Detection Limits on sub-GeV Dark Matter from XENON10*, Phys. Rev. Lett. **109**, 021301 (2012), [arXiv:1206.2644v1].

[63] E. Aprile et al. (XENON Collaboration), *First Dark Matter Search Results from the XENON1T Experiment*, Phys. Rev. Lett. **119**, 181301 (2017), [arXiv:1705.066551].

[64] Goldanskij V. I., Nikitin Yu. P., Rozental I. L., *Kinematic Methods in High-energy Physics*.